npj | materials degradation

Article

Published in partnership with CSCP and USTB

https://doi.org/10.1038/s41529-025-00644-0

Radiation-resistant Ti/BN coatings: insights from 171 days exposure to space radiation and atomic oxygen in low orbit

Abhijith Kunneparambil Sukumaran[1], Sara Rengifo[2], William Scott[2], Annette Gray[2], Miria Finckenor[2], Rony Thomas Murickan[1], Justin McElderry[2], Matthew Mazurkivich[2], Michael Renfro[3], Sang-Hyon Chu[4], Cheol Park[4], Anna Wu[4], Yifei Fu[5], Sudipta Seal[5] & Arvind Agarwal[1] ✉

Atmospheric Plasma Spray (APS) and Vacuum Plasma Spray (VPS) techniques were used to develop Ti/2 vol.% hBN coatings, for extreme space environments and tested aboard the International Space Station as part of the MISSE-17 (Materials International Space Station Experiments) program. The coatings were exposed to atomic oxygen, space radiation, and low-orbit thermal cycling. VPS coatings showed a 56% increase in microhardness, a 26% rise in elastic modulus, minimal porosity and crack density changes compared to APS coatings. The change in mechanical properties is attributed to the formation of TiO, TiO_2 and TiN from nitrogen retention, alongside radiation-induced dislocations, which enhanced surface hardening. The oxidation of titanium led to the formation of TiO and TiO_2, while boron nitride was retained and underwent transmutation in VPS coatings. XPS and EDS analyses confirmed the enhanced space-environment resistance of VPS coatings, making them ideal for long-term spacecraft protection in lunar and Martian conditions.

The increasing reliance on space exploration, satellite communications, and space-based research has brought to light the critical need for advanced materials capable of withstanding the unique and harsh conditions of space. The critical structural components of space shuttles and rovers are made of lightweight alloys such as Al 6061 and Ti6Al4V[1–6]. They often prematurely fail in these harsh conditions of space, such as extreme thermal fluctuations (−196 to 150 °C)[7], ionizing space radiations such as SPE: Solar Particle Events, GCR: Galactic Cosmic Rays[8] and secondary radiations (neutrons) that cause brittle fracture (Fig. 1). Also, sharp abrasive regolith that they encounter in Lunar and Martian terrains, causes severe abrasive and erosive material damage[9–11]. Hence, it is critical to develop strong and durable protective materials without compromising the payload limitations for future aerospace missions, such as Artemis and Luna, to establish a long-term presence on the Moon and Mars[12].

Hexagonal boron nitride (hBN) is known for its excellent wear resistance[13–15], high thermal conductivity (~550 W/m·K), and a wide coefficient of friction range (0.1–0.7) that strongly depends on the environment[13–15]; while friction is high under ultra-high vacuum (~0.7), it decreases significantly in humid or hydrocarbon-rich atmospheres due to enhanced basal plane slip and tribochemical film formation[15].Hexagonal boron nitride (hBN) shares a structural similarity with graphene, featuring a two-dimensional lattice composed of boron (B) and nitrogen (N) atoms. While strong covalent bonds secure the atoms within each layer, the layers are interconnected by weak van der Waals forces[14–18]. This unique atomic arrangement allows the layers to shear easily during sliding, effectively reducing friction under abrasive conditions. Notably, the boron atoms in hBN exhibit a high thermal neutron absorption cross-section (~760 barns)[19], which is 200,000 times greater than that of graphene (C~0.0035 barn) and significantly surpasses conventional shielding materials like concrete[20]. Boron-containing nanomaterials and polymer composites have been widely studied for their ability to mitigate radiation and thermal hazards[13,17,21,22]. Recent research has focused on boron nitride nanotubes (BNNTs) for their effective radiation-shielding properties[18,23]. Assessments using the OLTARIS (Online tool for the Assessment of Radiation in Space) have shown that BNNTs provide strong protection against GCR and SPE while also acting as carriers for hydrogen absorption[21]. Additionally, research has revealed that enhancing a polyimide matrix with hBN nanoflakes can increase wear resistance by 70% while improving the mass absorption coefficient and radiation shielding by a factor of 2.2[13]. Likewise, titanium composites reinforced with BNNT and fabricated through spark plasma sintering demonstrated a 26% enhancement in wear

[1]Plasma Forming Laboratory, Florida International University, Miami, FL, USA. [2]Materials Test, Chemistry and Contamination Control Branch, National Aeronautics and Space Administration Marshall Space Flight Centre, Huntsville, AL, USA. [3]Plasma Processes, LLC, Huntsville, AL, USA. [4]Advanced Materials and Processing Branch, NASA Langley Research Center, Hampton, VA, USA. [5]Advanced Materials Processing and Analysis Centre, Nanoscience Technology Center, University of Central Florida, Orlando, FL, USA. ✉e-mail: agarwala@fiu.edu

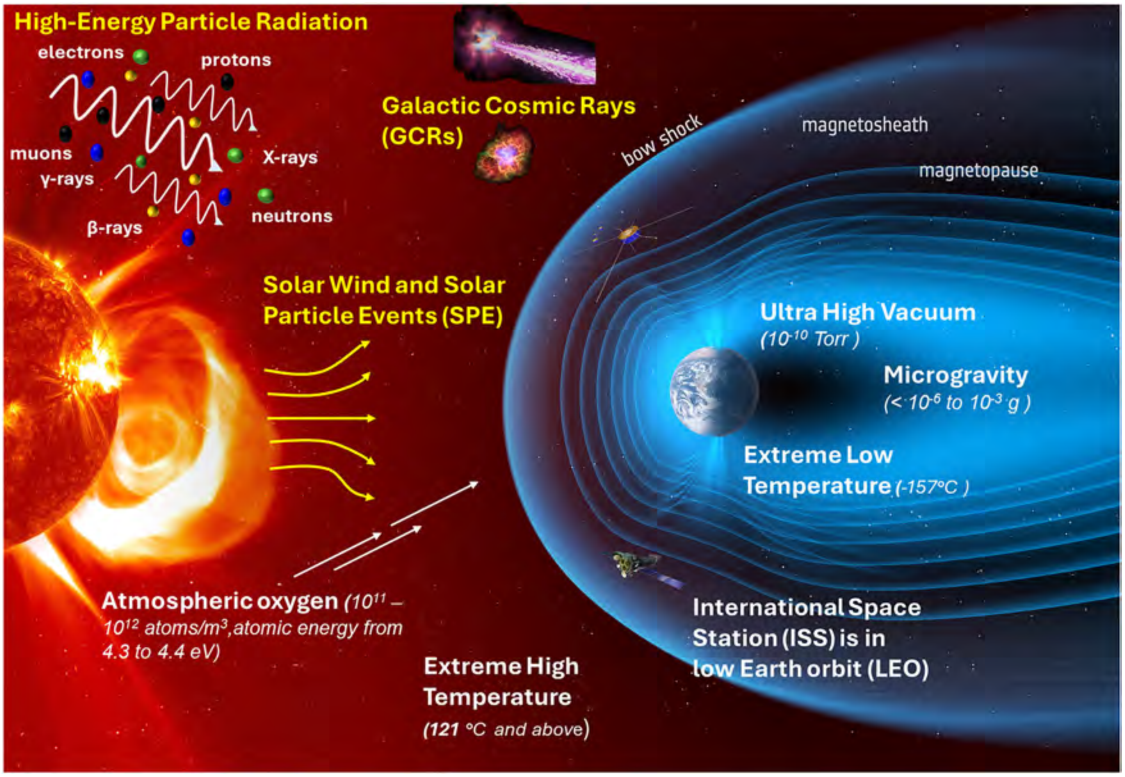

Fig. 1 | Schematic diagram illustrating the characteristics of the harsh space environment. (Source of the background image is used with permission from ESA/ATG Medialab)© ESA/ATG Medialab.

resistance and a 50% boost in neutron shielding with just 1 wt.% BNNT addition[18]. Moreover, a multilayer composite of polyethylene and hBN, fabricated using hot pressing, exhibited enhanced neutron shielding efficiency of up to 40% with 30 wt.% hBN, while also facilitating efficient heat dissipation during neutron interactions[22].

Because of these excellent multifunctional properties, we proposed novel multifunctional Ti/2vol.% hBN composite coatings by APS and VPS (Atmospheric and Vacuum Plasma spray) in our previous studies to counter harsh space environments[24–26]. Our initial study demonstrated that Ti/2 vol.% hBN coatings enhance abrasive wear resistance by 90% when tested against lunar regolith JSC-1A while also improving neutron radiation shielding efficiency by 27% under laboratory conditions[24]. In the second study, these coatings were exposed to simulated extreme lunar conditions, including thermal cycling, electron radiation, and combined electron radiation-thermal cycling. The results showed up to a 90% reduction in wear and a 28% improvement in neutron shielding, which was attributed to enhanced neutron capture by the ^{10}B isotope in the synergistic environment[25]. To assess their multifunctional feasibility, the coatings underwent erosion testing on a custom-built planetary erosion rig at extreme lunar temperatures (−196 to 150 °C). Results showed superior erosion resistance across all temperature conditions, attributed to their plasticity and high hardness compared to the Ti substrate, making them ideal candidates for multifunctional protective coatings for aerospace applications[26]. Owing to their exceptional multifunctional properties, Ti/2 vol.% hBN coatings deposited via APS and VPS were chosen for exposure testing in the MISSE-17 (Materials International Space Station Experiment). The experiment was conducted aboard the International Space Station (ISS) in 2023. Samples with the coatings were launched on SpaceX-27 on March 15, 2023, and MISSE Science Carrier (MSC) with the coated samples were installed on MISSE Flight Facility (MISSE-FF) outside of ISS to be exposed to space radiation, UV, and atomic oxygen, specifically under conditions of galactic cosmic rays and solar particle events in the Zenith direction for a duration of 171 days. After spending a total of 282 days in space from launch to return, completing 4512 orbits and covering 115 million miles, the coatings returned to Earth aboard SpaceX-29 on December 22, 2023. *Hence, this study aims to investigate the microstructural, phase, surface chemistry, and nanomechanical properties of coatings exposed to long-term space conditions in Low Earth Orbit (LEO)*[27,28]. This study uniquely evaluates these coatings under long-term space conditions, providing insights not achievable through laboratory conditions[28]. This scientific knowledge provides critical insights into the coating performance, helping to evaluate their feasibility for future aerospace and planetary missions.

Results and discussion

Post-exposure mass loss and microstructural integrity of coatings

Figure 2 presents a comparative analysis of APS and VPS Ti/2 hBN coatings (M3 and M4 are used for representation) before and after exposure to the space environment aboard the ISS. The backlit high-quality photographs are used to detect any potential surface impurities or contamination.

Post-exposure images reveal no visible signs of contamination, space debris, or micrometeoroid impact on the surface, suggesting that the samples were not subjected to any significant deposition of space impurities. The corresponding pre-flight and post-flight top surface SEM images provide detailed insights into the microstructural integrity of the coatings. Both SEM images show consistent surface features with no visible signs of degradation, microcracks, or defects after exposure, indicating good coating integrity. This confirms that the coatings remained intact and unaffected by the harsh conditions in space, retaining their microstructural stability. The exposed samples showed a slight increase in roughness, but the change is not substantial enough to be significant to alter any mechanical or tribological properties (Table 1). The observed differences between pre- and post-exposure specimens are likely due to specimen location-to-location variations rather than the effects of exposure itself.

Figure 3a and b represent cross-sectional SEM images of Ti/2 vol.% hBN coatings applied via APS (left) and VPS (right) processes exposed in

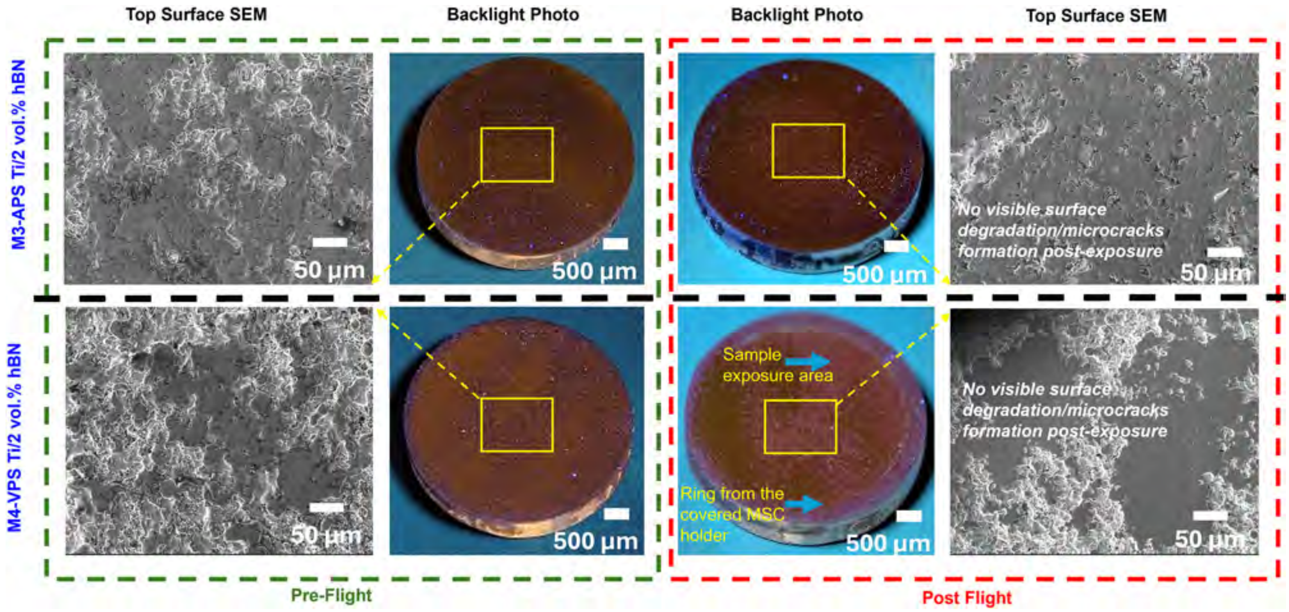

Fig. 2 | Comparison of pre-and post-flight top surface SEM images and backlight of M3-APS and M4-VPS Ti/2 vol.% hBN coatings. Backlight images show no visible surface degradation or contamination, though a surface ring from the mounting process on the MSC carrier is present on the VPS sample. SEM images do not show any craters, defects, or contamination from space debris. (Note: SEM images are from different areas of the surface).

Table 1 | Surface roughness of samples post-exposure on the ISS

Sample	Pre-Flight (μm) (Avg ± SD)	Post-Flight (μm) (Avg ± SD)	Flight percent change in roughness (%)
M3-APS Ti/2 hBN	3.47 ± 0.01	3.80 ± 0.92	9.51
M4-VPS Ti/2 hBN	3.85 ± 0.49	4.01 ± 0.75	4.15

space. In Fig. 3a, the unexposed side (Side B) exhibits a minor microcrack network but no significant structural damage, indicating that both coatings maintained their integrity in the absence of harsh environmental exposure. However, Fig. 3b, which shows the exposed side (Side A), reveals a marked increase in open porosities and cracks, particularly in regions directly impacted by space radiation. The yellow arrows emphasize these defects, highlighting the areas where the coatings have degraded. This degradation can be attributed to the harsh conditions in space, especially prolonged exposure to irradiation, which likely led to the formation of dislocations within the material structure[25,29].

Temperature change of samples from the underdeck sensor from April to September 2023 is plotted in Fig. S1. The highest recorded temperature on the mount side during September was 43.75 °C, while the lowest on the swing side was −29.75 °C. The average temperature range on the mount side was 7–37 °C, and for the swing side, it was 0-30 °C. (Note: "Mount side" refers to the surface attached directly to the MISSE-FF platform, while "swing side" refers to the side exposed outward toward space.) From April to September, there was an average temperature increase of approximately 10 °C. Although previous studies show that the temperature range outside is much higher, typically between −150 °C and 120 °C[30], the measured fluctuation was only −30 °C to 44 °C, significantly lower than anticipated, likely due to the MISSE-FF body maintaining a relatively stable temperature and the less-than-ideal thermocouple location. Coatings undergo cyclic thermal stress due to these temperature changes, which can lead to potential microstructural changes. These stresses, combined with radiation damage, may have exacerbated the cracking and porosity formation, compromising the microstructural integrity of the coatings. Figure 3c indicates a comparison of crack density (red) and porosity density (blue) for exposed and control samples, further highlighting this behavior. The APS-exposed samples show a significant 21% increase in crack density, along with a 50% increase in porosity, while the VPS-exposed samples exhibit little or no increase in crack density and a 19% increase in porosity. SEM images of the APS coatings (Fig. 3d), processed using ridge detection in Python, clearly reveal a higher crack density in the exposed samples compared to the control, reinforcing the conclusion that space exposure leads to increased microstructural damage. A similar study conducted in our research group under controlled laboratory conditions[25] observed and confirmed the same phenomena, indicating enhanced porosity and crack formation. This was attributed to radiation-induced brittle fracture, combined with cyclic thermal stress, which exacerbated the material's susceptibility to structural degradation. The comparison between APS and VPS coatings suggests that both experienced structural damages, though the severity varies slightly, likely due to differences in the initial microstructure formed during the coating process. These findings align with the laboratory conditions[25], demonstrating that both radiation and cyclic thermal stresses contribute to crack propagation and increased porosity in the coatings, leading to microstructural disintegration.

Influence of exposure and atomic oxygen on coating phase composition

XRD analysis was performed to investigate the effects of space irradiation and atomic oxygen on the phases of the thermal sprayed coatings (Fig. 4a). The as-sprayed coatings predominantly consist of Ti and TiO as major phases, along with TiB and TiN, formed because of the reaction of hBN during the plasma spray process. Previous research has demonstrated that a significant amount of metastable TiO phase is produced during spraying, with approximately 80% TiO in APS coatings and 30% in VPS coatings, due to the vacuum conditions used in VPS[24]. Furthermore, Raman spectroscopy from earlier studies confirmed the presence of hBN (~1365 cm^{-1}) in the coatings, as well as TiNx (150–300 cm^{-1}), TiO_2 (rutile), and TiB (550–600 cm^{-1}), providing a detailed phase characterization of the coatings' composition. Similarly, the XRD analysis in this study shows the same

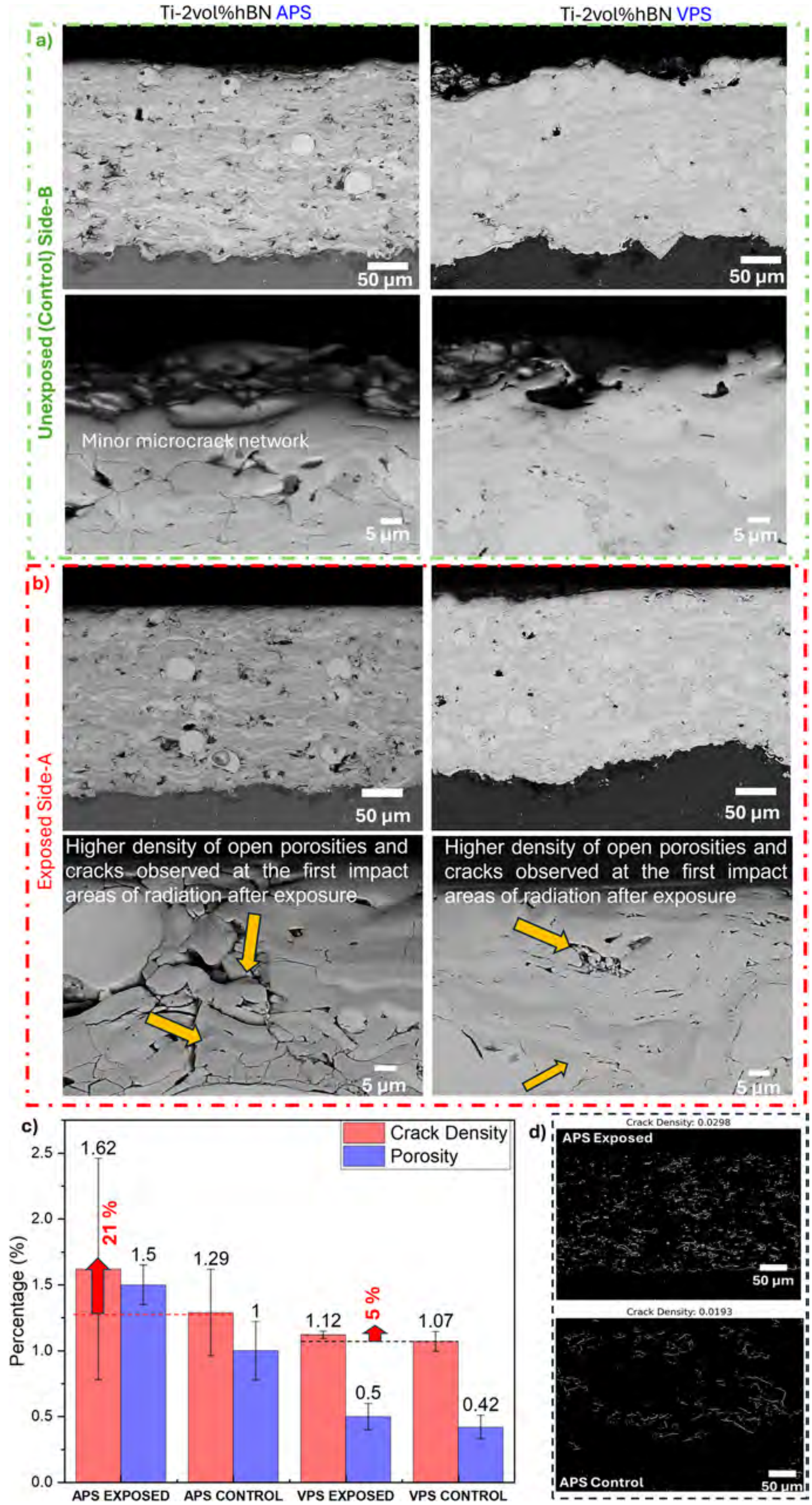

Fig. 3 | Cross-sectional SEM images and crack density of Ti/ 2 vol.% hBN coatings by APS (left) and VPS (right). **a** The unexposed side (Control, Side B) shows a minor microcrack network with no significant structural damage. **b** The exposed side (Side A) shows a higher density of open porosities and cracks in the radiation impact areas after exposure. Yellow arrows highlight the defects in the exposed coatings. **c** Comparison of crack density (red) and porosity density (blue) for exposed and control samples. APS-exposed samples show a 21% increase in crack density, while VPS-exposed samples show a 5% increase. **d** SEM images of APS coatings, processed using ridge detection, reveal higher crack density in exposed samples compared to control samples due to the effect of exposure.

characteristic peaks for Ti and TiO as the major phases, with slight variations in peak intensity. These variations are likely due to the diffusion of atomic oxygen during exposure, which may have subtly altered the phase composition or structure of the coatings. To quantify this variation, the Rietveld analysis performed on the exposed and control samples is represented in Fig. 4b. The data shows a clear increase in oxide phases (TiO) in both APS and VPS coatings after exposure, with a 7% increase in APS coatings and a more pronounced 25% increase in VPS coatings. This rise is likely due to exposure to atomic oxygen in the space environment, which accelerates oxidation. Figure 4c schematically represents the effect of atomic

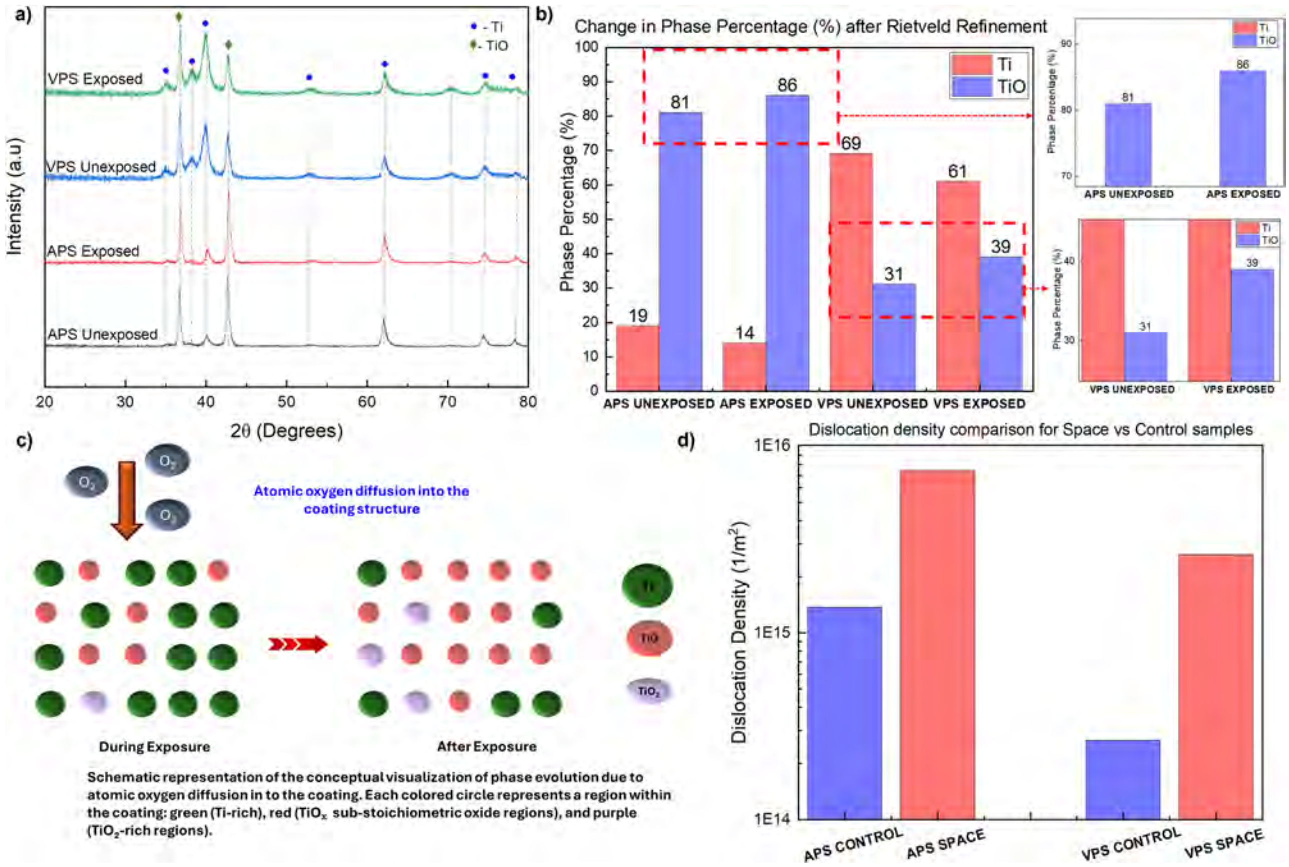

Fig. 4 | XRD analysis of exposed and control coatings. a XRD profileshowing major phases in the coatings. **b** Rietveld refinement indicates a higher phase percentage in TiO phase formation and reduction in titanium compared to the control sample, possibly due to the effect of atmospheric oxygen diffusion into the Ti matrix. **c** Schematic representation of oxidation progression in a Ti-based coating. Each colored circle represents a region within the coating: green (Ti-rich), red (TiO_x substoichiometric oxide regions), and purple (TiO_2-rich regions). The schematic is not to scale and is intended for conceptual visualization of phase evolution due to atomic oxygen diffusion. **d** Comparison of dislocation density in space vs. control samples using Williamson-Hall method.

oxygen diffusion into the coating structure. Highly reactive atomic oxygen (O) molecules diffuse into the microstructure of the thermal sprayed coatings, interacting with the existing phases of titanium (Ti) and titanium monoxide (TiO), resulting in two possible distinct chemical reactions (Eqs. 1 and 2).

$$Ti(s) + O^{\cdot}(g) \rightarrow TiO(s) \quad (1)$$

$$TiO(s) + O^{\cdot}(g) \rightarrow TiO_2(s) \quad (2)$$

These reactions illustrate how atomic oxygen (highly reactive oxygen radical), being more reactive than molecular oxygen, accelerates the oxidation of titanium, leading to the rapid formation of oxide layers such as TiO and TiO_2. This process is especially relevant in environments like space, where atomic oxygen is abundant and can lead to significant oxidation of exposed surfaces. The absence of TiO_2 in the XRD results could be due to its low concentration, formation in an amorphous state, overlapping diffraction peaks with other phases like Ti or TiO, or incomplete oxidation where the process stopped at TiO due to insufficient oxygen diffusion or exposure conditions. These factors make TiO_2 either undetectable or difficult to distinguish in the XRD analysis. The greater oxygen content in the VPS coatings post-exposure can be attributed to the vacuum plasma spray process, which initially produces coatings with lower oxygen content compared to APS. As a result, VPS coatings are more susceptible to oxidation when exposed to atomic oxygen, leading to a larger relative increase in oxide phases. Additionally, the microstructure of VPS coatings, formed under vacuum conditions, can allow localized penetration of atomic oxygen due to porosity or microcracks, leading to increased reactivity and a significant rise in oxide content. This analysis will be validated in upcoming sections through EDS and XPS, which are expected to confirm the presence of oxidized phases.

To examine the impact of dislocation caused by space irradiation from GCR and SPEs, dislocation densities were determined using crystallite sizes derived from the Williamson-Hall (WH) method (Eq. 3). Peak broadening was quantified by measuring the full-width at half maximum (FWHM) for each peak, which was obtained by fitting the XRD pattern with the Pseudo-Voigt function. The average crystallite size was obtained by fitting the graph of $\beta_{hkl} \cos\theta$ vs $4 \sin\theta$.

$$\beta_{hkl} \cos\theta = \frac{0.9\lambda}{D} + 4\varepsilon sin\theta \quad (3)$$

where, θ is the diffraction angle, β_{hkl} is FWHM, λ is the wavelength of $\mathrm{Cu}k_\alpha (\lambda = 0.154056nm)$, ε is the lattice strain and D is average crystallite size. Figure 4d presents the dislocation density results obtained from the linear fitting of the WH-plot. The dislocation density (ρ) is calculated by Eq. 4.

$$\rho = \frac{1}{D^2} \quad (4)$$

Figure 5d reveals a substantial increase in dislocation density by one order of magnitude in the space-exposed samples, attributed to lattice displacement of atoms caused by high-energy particle radiation[31–36]. This radiation-induced formation of black dot defects and dislocation clusters has been well-documented in previous studies[31,32,36], and similar effects were

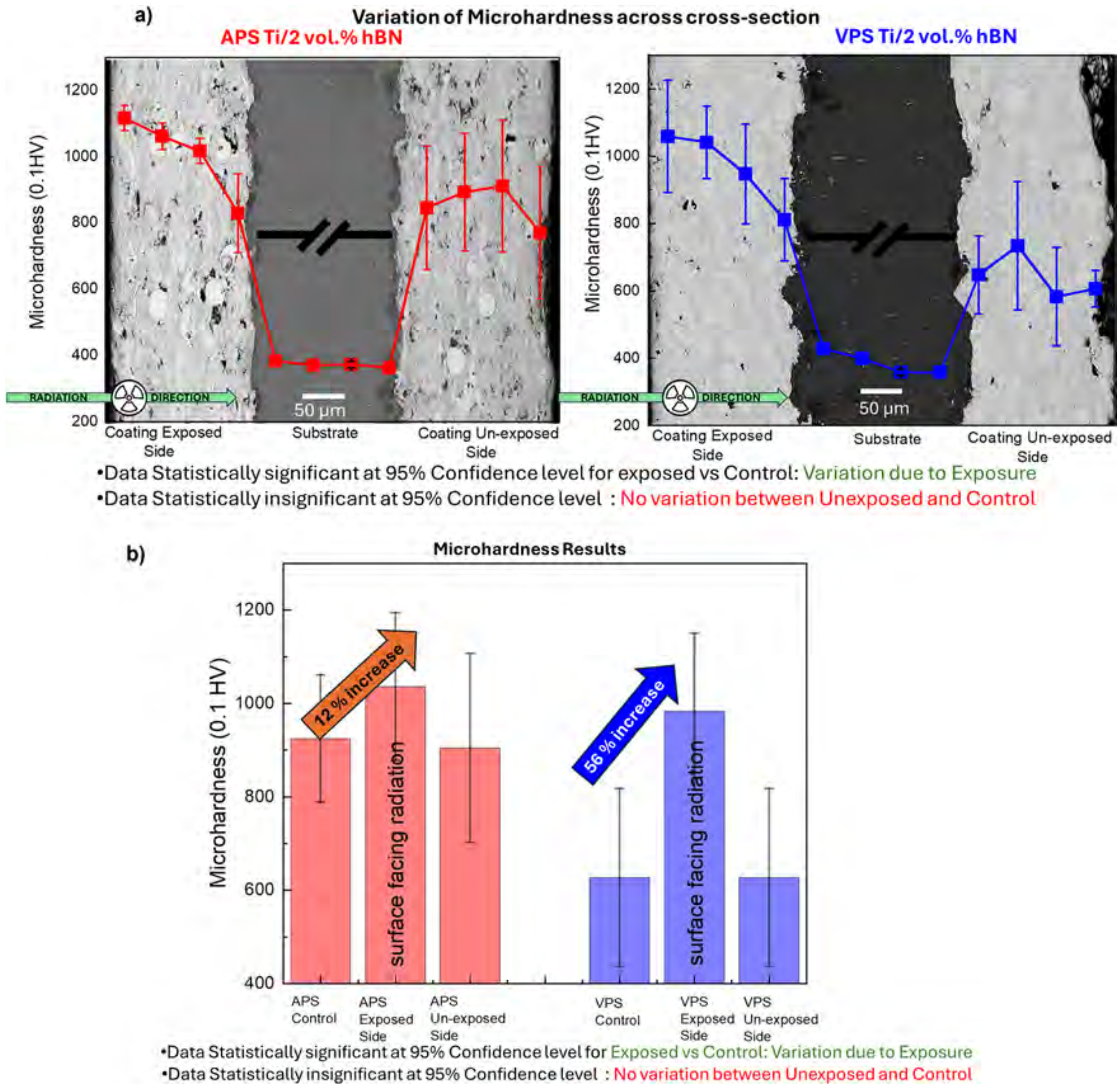

Fig. 5 | Microhardness property variation in the coatings. a Variation of microhardness across coating cross-section along the direction of radiation travel. **b** Microhardness comparison of APS and VPS exposed and control coatings.

observed in our prior research under pelletron irradiation in laboratory conditions, evidenced using bright-field TEM analysis[25]. The elevated dislocation density enhances radiation-induced hardening in the coatings. Consequently, the combined effects of increased oxide phase formation and higher dislocation density are expected to influence the overall mechanical properties of the coatings significantly.

Microhardness and nanomechanical properties of the coatings apropos of exposure

Fig. 5a shows the variation of hardness across the cross-section of APS (left) and VPS (right) Ti/2 vol.% hBN coatings due to radiation exposure. The data is plotted as hardness values across the thickness of the coatings, with the center representing the substrate surface. For both Ti/2 vol.% hBN coatings, the hardness is higher near the surface exposed to radiation, likely due to dislocation formation and atomic oxygen effects, such as TiO and TiO_2 phase formation. The higher standard deviation in the VPS coating is likely due to the significant 25% increase in TiO formation during exposure, resulting in uneven oxidation and greater variability in hardness. In contrast, APS coatings already had a higher initial TiO content, leading to more uniform oxidation and less variation in hardness across the coating. Also, the hardness could gradually decrease as radiation penetrates the coating due to the boron capture mechanism, where B^{10} isotopes absorb radiation and potentially prevent further penetration, thereby mitigating its impact on the deeper regions, as evidenced by our previous studies[13,18,21,22]. This results in a more stabilized hardness towards the unexposed side, which remains largely unaffected by radiation and shows similar data to that of the control sample. The comparative analysis of the microhardness response of the APS and VPS coatings before and after exposure is shown in Fig. 6b. In the APS coatings, the exposed surface (Side A) experienced a 12% increase in hardness compared to the control, indicating that the coating's structure was affected by radiation and reaction from atomic oxygen. In contrast, the VPS coatings showed a much more pronounced 56% increase in hardness on the surface exposed to a direct space environment. This substantial increase in VPS coatings suggests greater sensitivity to the space environment, likely due to a combination of enhancement in TiO phases as shown by XRD and from oxygen diffusion. Irradiation-induced hardening is likely caused by the penetration of radiation through the coatings, introducing dislocations into the atomic structure. Prior research on irradiation effects in metals and ceramics has demonstrated the development of point defects, dislocation loops and dislocation clusters[31–33,35]. Our previous research under laboratory conditions supports this, demonstrating a higher dislocation density in XRD, evident through the presence of dislocation clusters and black dot effects evidenced by TEM analysis[25]. The difference in the magnitude of hardness increase between APS and VPS coatings may also be related to

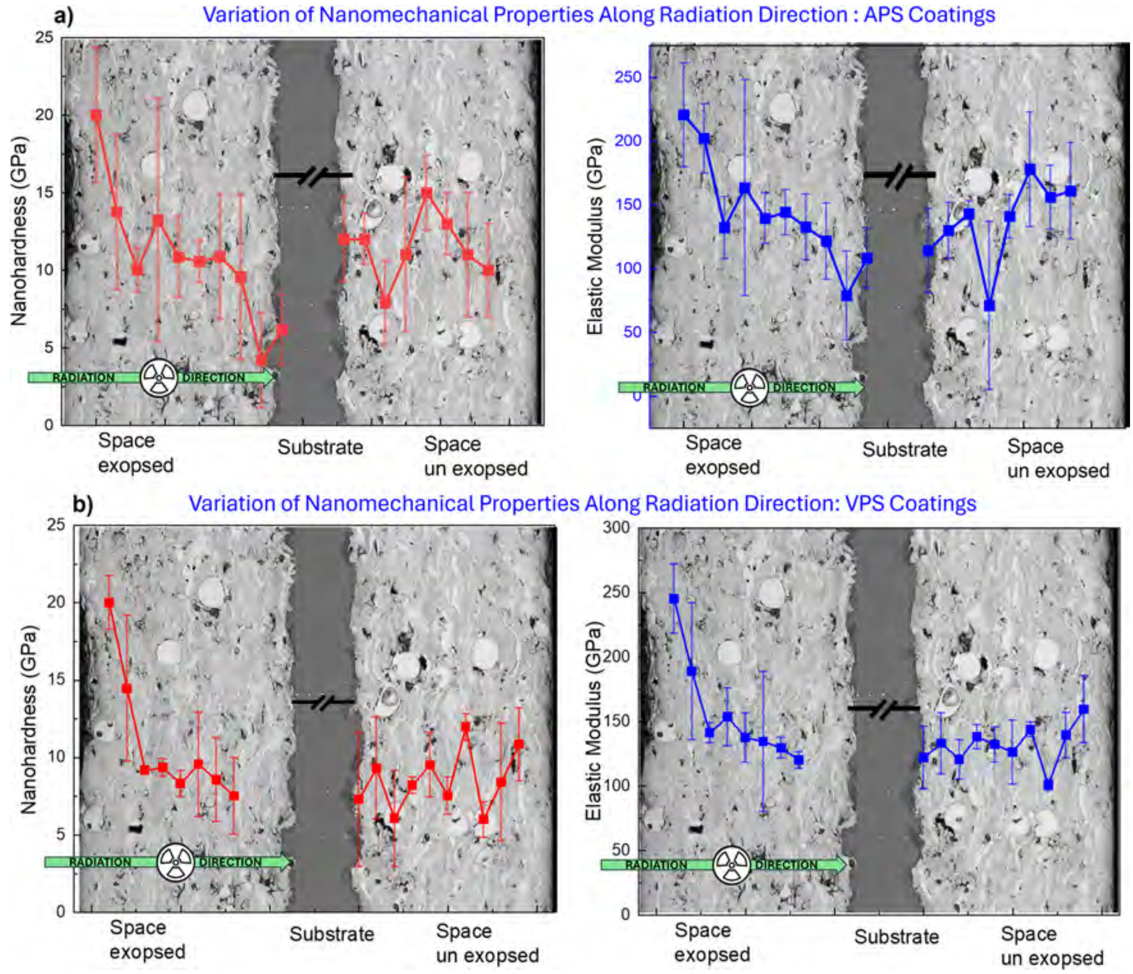

Fig. 6 | Nanomechanical response variation along the direction of radiation travel. **a** APS Coatings. **b** VPS Coatings.

Table 2 | Nanomechanical response of APS coatings from cross-section and top-surface

Surface	Sample	Nano-hardness (GPa) (Avg ± SD)	Elastic Modulus (GPa) (Avg ± SD)
Cross-section	Space Exposed (CS-A)	11.18 ± 5.7	153 ± 63
	Space Unexposed (CS-B)	10 ± 3	126 ± 29
	Cross-section Control	8.68 ± 4	118 ± 35
Top Surface	Space Exposed (TS-A)	9.3 ± 4.6	115 ± 38
	Space Unexposed (TS-B)	7.87 ± 3	110 ± 37
	Top-Surface Control	7.21 ± 2.7	100 ± 21

Statistical Significance using ANOVA at a 95% confidence level indicates:
Exposed vs Control: Variation due to Exposure: Statistically Significant at $P = 0.05$.
Unexposed vs Control: No Variation: Statistically Insignificant at $P = 0.05$.

differences in microstructural response to radiation and atomic oxygen. Both coatings maintained hardness on the unexposed side, with values nearly identical to the control, indicating that the changes in hardness are confined to the space-exposed surfaces. Statistical analysis using one-way ANOVA at a 95% confidence level reveals that for the exposed APS and VPS coatings, the observed variation is attributed solely to space exposure ($P > F = 0.03603$ for APS and 0.0001 for VPS). In contrast, under unexposed conditions, the variation is statistically insignificant ($P > F = 0.6997$ for APS and 0.24832 for VPS), indicating no measurable difference between the unexposed coatings and the control samples. This suggests that hBN plays a crucial role in absorbing radiation and facilitating boron capture, effectively shielding the material from radiation-induced damage on the unexposed side. The increased hardness is likely to improve the overall mechanical properties and resistance of the coatings in space environments.

The nanomechanical property assessment of the coatings post-exposure is captured in Fig. 6, and Tables 2 and 3. The comparison of load-displacement curves from nanoindentation tests performed on sample cross-sections (a-c) and top surfaces (d-f) for both APS and VPS coatings are presented in Fig. S2 and S3. Most of the load-displacement curves show smooth behavior during the loading, dwell, and unloading cycles.

However, sudden fluctuations are observed for some indents due to material heterogeneity, such as porosity or the formation of cracks caused by oxidation or dislocation-induced hardening, which leads to increased brittleness and disrupts the material's response during indentation. The corresponding nanomechanical response, including nano hardness and

Table 3 | Nanomechanical response of VPS coatings from cross-section and top-surface

Surface	Sample	Nano-hardness (GPa) (Avg ± SD)	Elastic Modulus (GPa) (Avg ± SD)
Cross-section	Space Exposed (CS-A)	9.75 ± 1.9	144 ± 19
	Space Unexposed (CS-B)	9.3 ± 2.6	134 ± 22
	Cross-section Control	8 ± 2.6	126 ± 21
Top Surface	Space Exposed (TS-A)	9.2 ± 2.4	142 ± 24
	Space Unexposed (TS-B)	8.6 ± 2	137 ± 22
	Top-Surface Control	7.3 ± 3	113 ± 36

Statistical Significance using ANOVA at a 95% confidence level indicates:
Exposed vs Control: Variation due to Exposure: Statistically Significant at $P = 0.05$.
Unexposed vs Control: No Variation: Statistically Insignificant at $P = 0.05$.

Table 4 | Calculated atomic elemental concentration by XPS

Elements	Sensitivity Factor	APS: Atomic Concentration (%)		VPS: Atomic Concentration (%)	
		Control	Space	Control	Space
Ti	Titanium (Ti 2p): 7.9	4.42	5.59	7.94	8.03
B	Boron (B 1 s): 0.486	58.26	48.71	38.91	33.45
N	Nitrogen (N 1 s): 1.87	21.51	24.65	29.69	35.76
O	Oxygen (O 1 s): 2.93	15.79	21.03	11.42	22.749

elastic modulus (in GPa), for the coatings, specifically the space-exposed side, space-unexposed side, and control, are tabulated in Tables 2 and 3. These responses are shown for cross-sections, and top surfaces for both APS and VPS coatings.

The nanomechanical responses for both APS and VPS coatings closely mirror the trends observed in microhardness measurements. Table 4 indicates a 30% increase in nano-hardness and elastic modulus for the APS coating's space-exposed side compared to the control sample on the cross-section. On the unexposed side, a smaller increase of 16% in nano-hardness and 7% in elastic modulus was measured, suggesting that radiation and atomic oxygen had minimal impact after traveling through the material. The higher standard deviation observed in nano-hardness and elastic modulus for APS space-exposed samples is influenced by the heterogeneous distribution of secondary phases, including TiO and TiO_2 formed through atomic oxygen exposure. Additionally, APS coatings often contain unmelted particles, porosity, higher crack density, and secondary phases like TiN and TiB, contributing to localized mechanical variations. These structural inconsistencies create regions of varying hardness and elasticity, leading to the observed increase in standard deviation. Statistical analysis confirmed that the differences between the exposed and control samples were statistically significant at a 95% confidence level ($P > F = 0.04848$ and 0.01963 for nano-hardness and elastic modulus, respectively), while the differences between the unexposed and control samples ($P > F = 0.14973$, and 0.39187 for nano-hardness and elastic modulus, respectively) were not and their responses are similar. This indicates that the effects of exposure are primarily limited to the surface directly exposed to space.

For the top surface, similar trends were observed, with a 30% increase in nano-hardness and a 15% increase in elastic modulus on the exposed side, while the unexposed side saw only a 10% increase in both properties. This further supports the conclusion that radiation and atomic oxygen primarily affect the exposed surface. The variation along the radiation travel direction (Fig. 6a) shows that both properties are highest on the side directly exposed to space and gradually decrease toward the center, indicating reduced exposure effects. The elastic modulus remains higher than nano-hardness, as expected, since the modulus reflects the overall stiffness of the material, while hardness measures resistance to localized deformation. It is generally expected that the elastic modulus will be significantly higher than the hardness for most engineering materials, because plastic deformation requires not only overcoming lattice stiffness but also dislocation motion or microstructural rearrangement, which occurs at higher applied stress concentrations. Typically, for many ceramics and hard coatings, H/E ratios range from 0.05 to 0.1, which supports this expected trend[37]. This data emphasizes that the effects of radiation and atomic oxygen are strongest on the exposed surface, with limited impact on deeper or unexposed areas due to the reduced penetration of both radiation and atomic oxygen.

Like APS coatings, Table 3 shows that from the cross-section of VPS coatings, a 22% increase in nano-hardness and a 14% increase in elastic modulus were observed for the space-exposed face compared to the control sample. In the unexposed face, a smaller increase of 16% in nano-hardness and 6% in elastic modulus was noted, indicating that radiation and atomic oxygen have a limited effect after penetrating through the material. For the top surface, a 26% increase in nano-hardness and elastic modulus was observed for the space-exposed face compared to the control, while the unexposed face showed an 18-20% increase in both properties. This again indicates that the effects of radiation and atomic oxygen did not deeply impact the unexposed side. The trends in the data suggest that surface hardening from space exposure was more pronounced on the exposed side. Statistical analysis again confirmed that the differences between the exposed and control samples were statistically significant at a 95% confidence level ($P > F = 0.01468$ and 0.00375) for nano-hardness and elastic modulus, respectively), while the differences between the unexposed and control samples were not and their responses were similar ($P > F = 0.089$ and 0.21) for nano hardness and elastic modulus, respectively). Like APS coatings, the variation of properties along the radiation travel direction in VPS coatings follows a distinct trend (Fig. 6b). The plot shows that nano-hardness and elastic modulus are highest on the left side, which was directly exposed to space radiation and atomic oxygen. As the scan progresses toward the center of the coating, both properties significantly decrease, indicating reduced radiation and atomic oxygen effects in this transition zone. On the right side, corresponding to the unexposed face, there is minimal variation, suggesting limited penetration of space environment effects into the material. This trend is likely due to the ability of the ^{10}B isotope to absorb radiation and undergo transformation into secondary particles, such as lithium and alpha particles, through the boron capture mechanism[13,19,21]. Effectiveness in radiation shielding could account for the reduced impact of radiation on the unexposed side, as it mitigates radiation penetration and minimizes structural changes deeper within the material.

The enhancement in nanomechanical properties on the exposed side is likely attributed to two main factors. The first is radiation-induced dislocations, which have been well-documented in previous research[25]. The second factor is the exposure to atomic oxygen, which diffuses through the coating layers, contributing to changes in the material's structure and properties. In low Earth orbit (LEO), where atomic oxygen (O) is abundant[28,38], the potential reactions in Ti/2 vol.% hBN coatings can be categorized into two main sections. These reactions depend on factors such as temperature, oxygen concentration, and exposure time, which influence the feasibility and extent of these reactions. In addition to Eqs. 1 and 2, which form TiO and

TiO_2, the other major reaction could be

$$4BN + 6O^{\cdot} \rightarrow 2B_2O_3 + 2N_2 \tag{5}$$

and based on concentration and environmental factors, minor reactions such as,

$$2TiN + 3O^{\cdot} \rightarrow 2TiO_2 + N_2 \tag{6}$$

$$TiB + O^{\cdot} \rightarrow B + TiO \tag{7}$$

$$2B + 3O^{\cdot} \rightarrow B_2O_3 \tag{8}$$

$$4Al + 6O^{\cdot} \rightarrow 2Al_2O_3 \tag{9}$$

$$4V(s) + 5O^{\cdot} \rightarrow 2V_2O_5 \tag{10}$$

While reactions 7-10 are unlikely under normal Earth conditions, in high reactive atomic oxygen environments such as LEO or at elevated temperatures, oxidation can progress further, leading to the formation of B_2O_3[39–41] and secondary oxides like Al_2O_3 and V_2O_5[42] typically formed in layers with TiO and TiO_2 being the primary oxide due to its abundance in the alloy. The formation of oxide phases such as TiO_2, Al_2O_3, and B_2O_3 enhances the nanomechanical properties of the coatings, increasing both hardness and elastic modulus (stiffness). The ceramic nature of these phases contributes to a noticeable increase in surface hardness, while the stiff oxides also raise the elastic modulus, making the coating more rigid. However, this comes at the cost of increased brittleness, which can lead to micro-cracking under mechanical stress, as evidenced by the higher crack density on the exposed side (Fig. 3d). Overall, oxidation results in a harder, stiffer coating on the exposed side, albeit with reduced ductility and increased brittleness as evidenced by their nanomechanical responses.

Investigation of atmospheric oxygen effects on coatings via EDS and XPS analysis

To evidence and quantify the effects of atomic oxygen penetration and diffusion into the coating interlayers, a high-resolution EDS line scan (Fig. 7) and to understand the surface chemistry of coatings, a high-resolution XPS analysis (Fig. 8) was conducted. The EDS line scan across the cross-section of the APS Ti/2 vol.% hBN coating in Fig. 7a reveals significant oxidation from the exposed to the unexposed side. A high oxygen signal on the exposed side indicates the formation of oxides, possibly TiO, TiO_2, and B_2O_3, correlating with the presence of titanium and boron. Peaks in titanium and oxygen suggest that Ti has oxidized to TiO and TiO_2, while variations in boron and nitrogen levels point to the oxidation of BN to B_2O_3[39–41], contributing to changes in the mechanical properties, as explained in section 3.3. The formation of these oxides increases hardness and stiffness but also leads to brittleness, potentially explaining the higher crack density on the exposed side. The higher oxygen intensity on the exposed side, coupled with the non-uniform oxygen distribution on the unexposed side, highlights a clear disparity in oxidation levels. The microhardness trend on the exposed side mirrors the nano-hardness and elastic modulus, indicating consistent mechanical behavior across this region. In contrast, the unexposed side remains largely unaffected due to limited oxygen penetration, resulting in minimal changes to its mechanical properties compared to the control samples, as previously discussed. The line scan data aligns with XRD results, confirming that surface oxidation from space exposure on the exposed side contributes to the enhanced mechanical properties observed.

The Raman spectrum (Fig. 7b) reveals that both VPS and APS coatings contain phases such as TiO, TiO_2, TiN, and B_2O_3, with B_2O_3 peaks being particularly prominent in samples exposed to space. Peaks observed around 910–1000 cm^{-1} imply the formation of complex titanium borate oxides (such as TiB_2O_3), likely as a result of high-temperature conditions. Space exposure, particularly in the presence of atomic oxygen, may have further contributed to this oxidation process. Additionally, carbon impurities indicated by the D-band at 1340 cm^{-1} and the G-band at 1580 cm^{-1} may stem from the grinding of samples prior to exposure.

Since the characteristic hBN peak was not observed in Raman spectra after space exposure, XPS analysis was further employed to understand the effect of space exposure on BN chemical states and depth of oxidation within the coating (Fig. 8). Survey and High-resolution XPS spectra of APS and VPS coating samples comparing major elements boron (B1s), oxygen (O1s), Nitrogen (N1s), and Titanium (Ti2p) regions are represented by Fig. 8a and b respectively.

In this study, binding energy calibration was performed using the adventitious C 1s peak to maintain internal consistency across all samples. However, we acknowledge that this method introduces a systematic uncertainty of approximately ±0.2–0.4 eV[43]. This limitation is particularly significant when attempting to distinguish between closely spaced chemical environments, such as N–B and N–Ti. As such, our interpretation of the nitrogen bonding states accounts for this uncertainty, and conclusions are drawn with appropriate caution.

The low intensity of the B 1s signal in APS and VPS samples is speculated to be transmutation of boron into lithium and other secondary particles through radiation absorption. Lithium was not detected in space-exposed APS and VPS samples, likely due to several factors, including surface contamination or oxidation forming a masking layer, lithium diffusing into the bulk material or reacting to lower its surface concentration, or the concentration being below XPS detection limits[44,45]. The deconvoluted XPS spectra for the space-exposed APS and VPS coatings provide insights into the chemical states of titanium and nitrogen in both coatings (Fig. 8b and c). In the APS coating, the Ti2p spectrum shows peaks for Ti^{4+}-O (titanium dioxide) and Ti^{3+}-O, indicating significant oxidation of titanium during space exposure[46] In contrast, the VPS coating also shows oxidized titanium with Ti^{4+}-O and Ti^{3+}-O peaks[47] but additionally features a Ti-N peak, indicating the formation of titanium nitride (TiN)[48]. The space environment may have favored nitride formation in VPS samples, further enhancing the mechanical response by the harder ceramic phase. The N 1s spectrum reveals the presence of N_2 (nitrogen gas) and N-B (boron nitride), confirming the retention of boron nitride in the coating after space exposure[41]. hBN was identified at 398 eV in the XPS N1S spectrum (Fig. 8d), showing a higher intensity for VPS coatings and a lower intensity for APS coatings. In space-exposed samples, a reduction in intensity at this 398 eV peak was observed compared to control samples, suggesting some level of oxidation to B_2O_3 and the formation of complex titanium borates under the influence of atomic oxygen. However, both coatings have retained a significant amount of BN within the samples despite the exposure[49]. Overall, the APS coating exhibits more oxidation, while the VPS coating demonstrates more nitride formation, which improved microhardness and nanomechanical properties as evaluated and could enhance the wear resistance. These differences highlight how the space environment impacts the chemical and mechanical properties of the coatings, depending on the original processing conditions.

The relative atomic concentration of elements from XPS spectra was calculated after peak area calculation by deconvolution (deconvoluted O1s spectra of APS and VPS coatings used for atomic concentration calculation[50] of oxygen) and applying sensitivity factor correction using ALSCOF database[44,45,51]. The relative atomic concentration for major elements was calculated using Eq. 11 and tabulated in Table 4. The relative atomic concentration analysis, coupled with nanomechanical property changes, reveals significant insights into the effects of space exposure on both APS and VPS coatings. For APS coatings, a 6% rise in oxygen and a 10% drop in boron suggest atmospheric oxidation and possible boron transmutation via the boron capture mechanism during exposure. This is accompanied by increased hardness and elastic modulus, as the formation of oxides such as TiO, TiO_2, and B_2O_3 strengthens the surface but also increases brittleness. The increase in titanium from 4.42% to 5.59% is likely to result from surface layer erosion, enriching the surface with titanium (Ti^{3+} and Ti^{4+}), which contributes to the enhanced mechanical properties[28]. Boron content

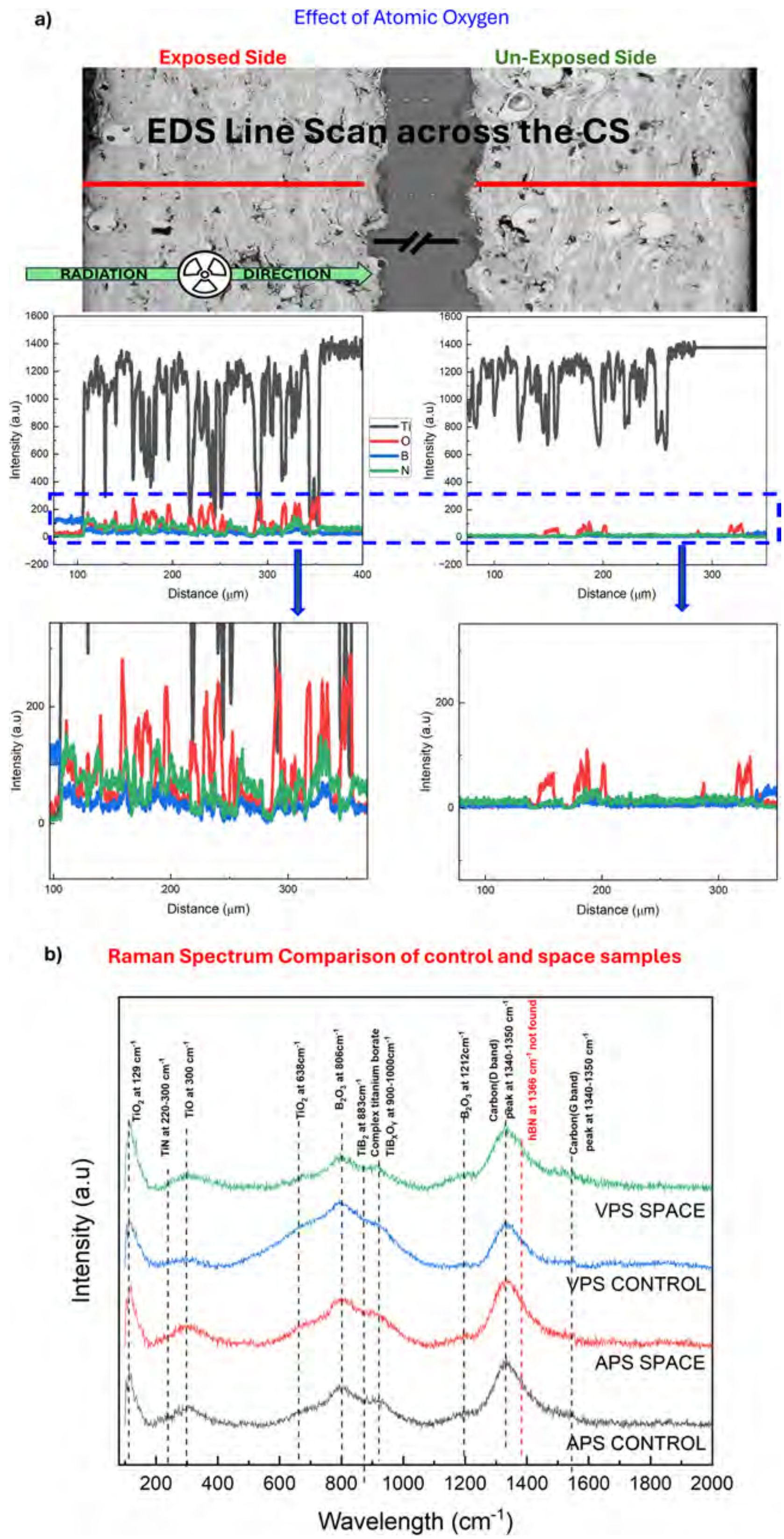

Fig. 7 | Surface chemistry analysis of coatings. **a** EDS line scan across APS Ti/2 vol.% hBN coating, revealing high and uniform oxygen peak intensity on the exposed side, in contrast to low and non-uniform oxygen distribution on the unexposed side, indicating atmospheric oxygen penetration from the exposed surface towards the unexposed side. **b** Raman spectrum comparison of space vs control samples.

decreased from 58% to 48%, likely due to sputtering, atomic oxygen erosion, and boron transmutation[28], which further influences the mechanical behavior by reducing the ductility of the coating. Nitrogen saw a slight increase from 22% to 25%, possibly due to surface depletion of other elements or external contamination (Fig. 9d), while oxygen increased from 15.79% to 21%, driving surface oxidation from atomic oxygen diffusion contributes to the observed enhancement in hardness. Similarly, for VPS coatings, an 11% rise in oxygen and a 6% drop in boron reflect similar processes of oxidation and boron transmutation. The slight increase in titanium from 7.94% to 8.03%, along with a drop in boron from 38.91% to

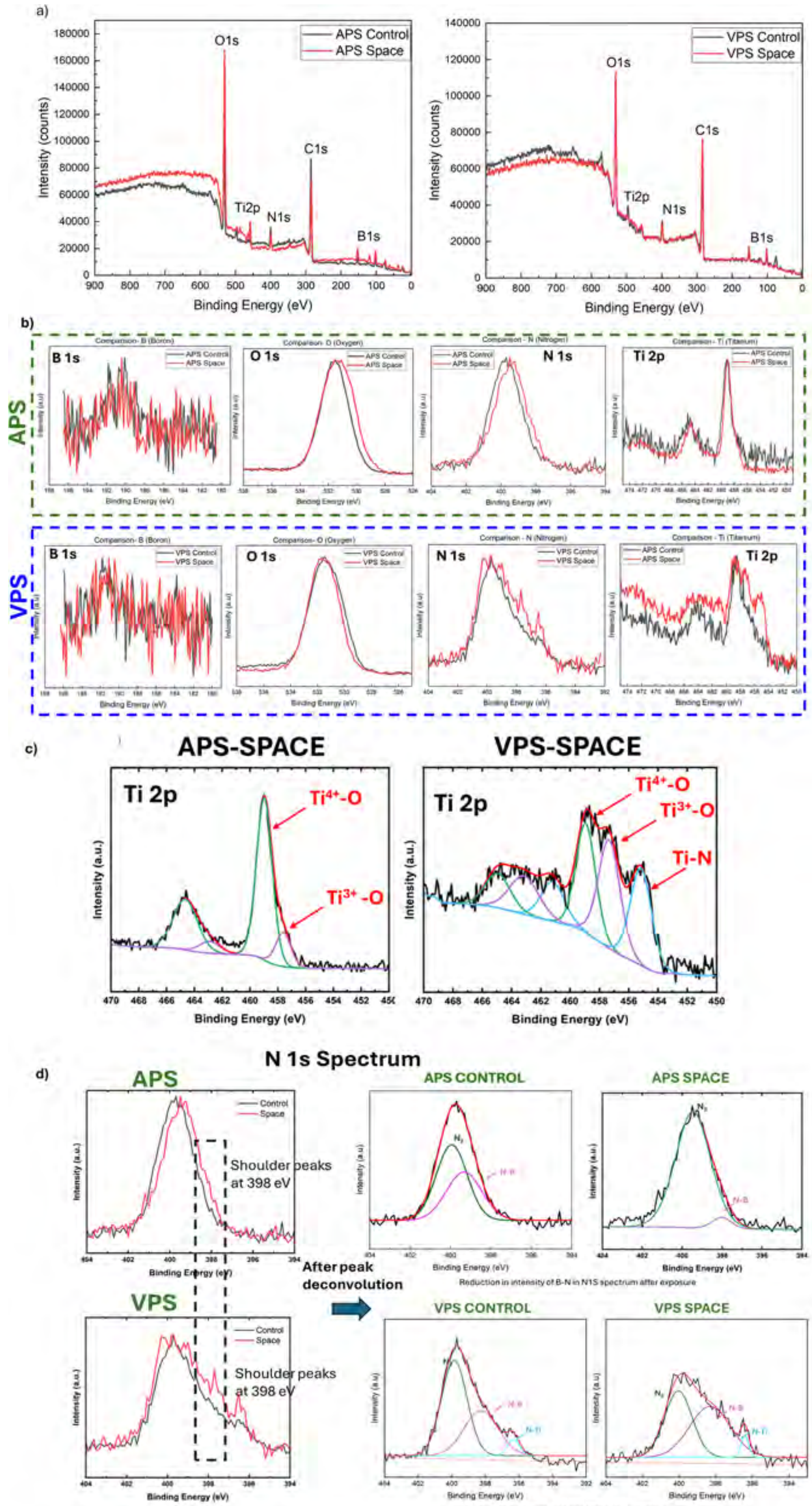

Fig. 8 | XPS analysis of coatings. **a** XPS survey spectra for APS and VPS Control and Space samples. **b** High-resolution XPS spectra of APS and VPS coating samples comparing major elements boron (B1s), oxygen (O1s), Nitrogen(N1s) and Titanium (Ti2p) regions (**c**) deconvoluted Ti2p region for APS and VPS space sample coating shows higher oxidation states of titanium (**d**) deconvoluted N1s region for APS and VPS coating shows retained BN in control and space coatings and formation of TiN phase.

33.45%, is likely due to space erosion and atomic oxygen effects, leading to enhanced mechanical properties such as increased hardness and stiffness. The significant rise in nitrogen from 29.6% to 35.76% and oxygen from 11.42% to 22.75% reflects further surface oxidation, which strengthens the coating but increases brittleness. Overall, these atomic concentration changes, combined with the enhancement in nanomechanical properties, illustrate the profound impact of space exposure, oxidation, and boron transmutation on the structural and mechanical performance of both APS and VPS coatings.

Based on this extensive analysis of atomic concentration changes and improved nanomechanical properties, both APS and VPS Ti/2 vol.% hBN coatings demonstrate excellent potential as candidates for structural

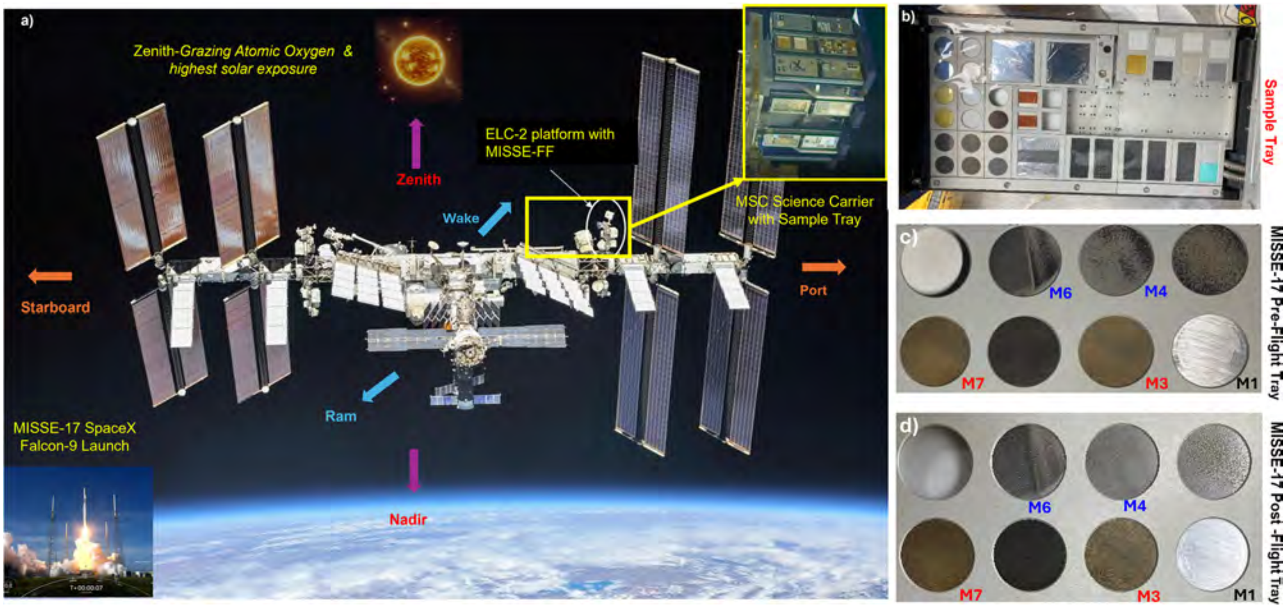

Fig. 9 | MISSE-17 Experimental pathway. a Visual representation of MISSE-17 flight test aboard the ISS starting from sample launch on SpaceX-Falcon 9 (Image courtesy: NASA. gov). The MISSE-MSC Flight carrier placed on the Zenith direction of ISS, inset: MSC Flight carrier box. **b** MSC-Sample tray with plasma sprayed coatings and substrate. **c** Pre-flight sample images (M1, M3, M4, M6, and M7) along with other MISSE samples. **d** Post-flight sample images (M1, M3, M4, M6, and M7) showing no visual degradation after exposure.

components in extreme space environments. The formation of oxides and nitrides leads to a significant increase in hardness and elastic modulus, which suggests enhanced wear resistance and improved durability under harsh space conditions such as atomic oxygen exposure and radiation. However, these changes may also reduce toughness and introduce interfacial stresses due to elastic modulus mismatch with the substrate. To fully evaluate these effects, wear testing on the same LEO-exposed samples is planned and will be presented in a forthcoming study[37]. The retention of mechanical integrity, coupled with their ability to resist oxidation and maintain surface stability, makes them ideal for applications where strength, durability, and resistance to environmental degradation are critical. Although the coatings experience some increase in brittleness, their overall performance enhancements in space environments position them as strong contenders for protecting and reinforcing structural components in long-term space missions.

Overall, this study presents a comprehensive evaluation of Ti/2 vol.% hBN composite coatings, deposited via APS and VPS, following 171 days of exposure to atomic oxygen and space radiation aboard the International Space Station. Both coatings demonstrated strong resistance to space-induced degradation, with the VPS coatings outperforming APS in mechanical integrity and structural stability. VPS samples showed substantial increases in microhardness (56%), elastic modulus (26%), and nano-hardness (22%), driven by the formation of oxide and nitride phases (TiO, TiO_2, B_2O_3, and TiN) resulting from atomic oxygen diffusion and radiation-induced effects.

Although APS coatings also exhibited mechanical improvements, their higher porosity and crack density suggest greater susceptibility to space environment damage. The minimal crack density increase in VPS coatings (only 5%) highlights their superior structural resilience. Surface chemical analyses (XPS and EDS) confirmed increased oxygen content and reduced boron concentration in both coatings, indicative of oxidative transformation and potential boron transmutation under radiation.

While some brittleness was observed post-exposure, particularly in APS coatings, the overall enhancements in hardness and stiffness, combined with maintained microstructural integrity, support the viability of these coatings for aerospace use. In particular, VPS Ti/hBN coatings emerge as strong candidates for protective applications on spacecraft and structural components exposed to harsh space environments, including LEO, Lunar, Martian, and deep-space missions, where resistance to wear, erosion, and radiation is critical.

Methods

Material preparation and coating deposition

Our previous research analyzed the effect of incorporating hBN at 2 and 10 vol.% into coatings[24]. The study revealed that a 2 vol.% hBN concentration was the most effective, significantly enhancing neutron shielding and wear resistance. A higher hBN content of 10 vol.% caused particle agglomeration and poor powder flowability during plasma spraying. Consequently, this compromised the structural integrity of the coatings[24].

In this work, Ti/2 vol.% hBN composite powder was produced through cryomilling. The raw materials consisted of hBN (sourced from Graphene Supermarket, with an average particle size of 5 μm, surface area of 7.5 m^2/g, and density of 2.1 g/cm^3) and Ti6Al4V (obtained from Tekna TEKMAT™ Ti64-45/16-G5, with an average particle size below 30 μm and a density of 4.5 g/cm^3; Additional details on cryomilling parameters and the coating fabrication approach are available in the section 1.1 of our prior publication[24]. For plasma spraying, circular pucks with a diameter of 3.81 cm and a thickness of 0.64 cm were machined from conventionally manufactured (CM) Al6061 and Ti6Al4V substrates. Atmospheric plasma spraying (APS) was carried out at Florida International University's Plasma Forming Laboratory, whereas vacuum plasma spraying (VPS) was performed at Plasma Processes, LLC, located in Huntsville, Alabama. Coatings were applied using an SG-100 plasma gun (Praxair Surface Technologies, Indianapolis, Indiana) on both sides of the substrates, ensuring a minimum thickness of 150 μm per side. The complete set of deposition parameters is presented in Table 5.

MISSE-17(Materials International Space Station Experiments) Exposure Testing

The Materials International Space Station Experiment (MISSE-17) aimed to evaluate the performance of various coatings under prolonged exposure to harsh space conditions[52]. Before launch, the coatings went to NASA Marshall Space Flight Center (MSFC) for preparation, where they underwent a Thermal Vacuum Chamber assessment at 60 °C and approximately 1.33 ×

Table 5 | Plasma spray process parameters[24]

Process Type	Spray distance (mm)	Feeding Type	Primary gas pressure (MPa)	Secondary gas pressure (MPa)	Carrier gas pressure (MPa)	Plasma power (kW)	Deposition time (s)	Vacuum level (MPa)
APS	140	External	0.28 (Ar)	0.55 (He)	0.21 (Ar)	22	90	NA
VPS	100	External	0.69 (Ar)	0.34 (He)	0.24 (N_2)	24	90	0.07

Table 6 | Samples and their nomenclature on MISSE Science Carrier (MSC) in MISSE- Flight Facility

Sample ID	Material
MERCRII 1 (M1)	Al6061 substrate uncoated on both sides
MERCRII 3 (M3)	Ti/ 2 vol%hBN APS coating applied on Al6061 substrate
MERCRII 4 (M4)	Ti/ 2 vol%hBN VPS coating applied on Al6061 substrate
MERCRII 6 (M6)	Ti/ 2 vol%hBN VPS coating applied on Ti6Al4V substrate
MERCRII 7 (M7)	Ti/ 2 vol%hBN APS coating applied on Ti6Al4V substrate

10^{-6} mbar for 24 hours to monitor outgassing, mass changes, and deformation, ensuring integrity before deployment. Launched on March 15, 2023, aboard SpaceX CRS-27 (27th Commercial Resupply Services mission of SpaceX), the coatings were installed on the MISSE Flight Facility (MISSE-FF) with assistance from the Canadian Space Agency (CSA) ISS Robotic Systems Team. The specimens were positioned on an external ISS platform facing the zenith direction directly away from Earth as seen in Fig. 9 and corresponding sample nomenclature is represented in Table 6.

The samples endured 171 days of exposure to harsh space conditions, including grazing atomic oxygen, galactic cosmic rays (GCR), intense UV radiation, solar particle events (SPE), high vacuum, and extreme temperature variations. Over the course of 282 days in space, they completed 4512 orbits and traveled an impressive 115 million miles. Only one side of the coated pucks was exposed to space conditions (named Exposed A side), while the unexposed side (Side B) remained in the MSC. The coatings were retrieved on September 22, 2023, and returned to Earth aboard Cygnus NG-19 on December 22, 2023, providing valuable data on long-term space exposure. The post-flight analysis involved measuring mass changes, offering insights into outgassing material degradation or debris deposition, and helping assess the coatings' durability for future aerospace applications.

Pre-and post-exposure microstructural characterization of coatings

The top surface and cross-sectional microstructural features of the coatings were analyzed to understand the effect of harsh space environments. The top surfaces were thoroughly analyzed using a scanning electron microscope (SEM) equipped with a secondary electron detector, a backscatter detector, and an energy-dispersive X-ray spectrometer (EDS) to examine microstructural and elemental variations following exposure. The control and exposed coatings were cut into sections, embedded in epoxy resin through cold mounting, and subsequently ground using 1200 grit SiC paper. For microstructural characterization, polishing was carried out with a 1 µm alumina suspension followed by a 0.05 µm colloidal silica suspension. SEM analysis, was conducted to examine the microstructure and cross-sectional features of the coatings. The thickness and porosity of the composite coatings were measured using ImageJ software. To ensure accuracy, ten randomly selected images of the polished cross-sections were analyzed, and the results were averaged to determine the final porosity and coating thickness. The crack density variation in the exposed and control coatings was analyzed using Python scripting and ridge detection algorithms to identify and quantify cracks on the material surface. High-resolution micrographs were pre-processed with OpenCV for noise reduction, and SciPy's ridge analysis was applied to detect elongated crack-like features. The total ridge length, representing cracks, was then normalized by the sample surface area to calculate crack density, ensuring accurate and reproducible results.

The phase composition and structural characteristics of the as-sprayed coatings were examined through X-ray diffraction (XRD) using a Rigaku Smart Lab system. Measurements were conducted with Cu $K\alpha_1$ radiation (λ = 1.54 Å) at a scanning speed of 2°/min. The instrument was operated at 40 kV and 40 mA, with data collected over a 2θ range spanning from 10° to 90°. The phase fractions and composition of atomic oxygen in the coatings were further deduced by Rietveld refinement using the Rigaku Smartlab software package.

Microhardness and nano-mechanical property variation in coatings

The Vickers microhardness of both as-sprayed and exposed coatings was evaluated using a LeCO LM810AT microhardness tester (USA). A load of 100 gf was applied with a dwell time of 15 seconds for each indentation. To determine the average microhardness, a minimum of ten indentations were performed across the polished cross-section. To evaluate the effect of space conditions on microhardness variation within the coatings, indentations were made along the width of the cross-section, spanning from the top of the exposed coating surface to the bottom of the unexposed side. This was repeated three times to ensure the accuracy and repeatability of data synthesis. This approach allowed for a comprehensive assessment of microhardness distribution through the entire sample thickness along radiation travel and oxygen penetration.

To evaluate the effects of irradiation and atomic oxygen on the exposed samples, nano-mechanical properties such as nano-hardness and elastic modulus were measured using a high throughput nanoindenter (NHT2 nanoindenter, Anton Paar, USA). A Berkovich diamond indenter tip was used for all measurements. The Oliver–Pharr method was employed to extract the reduced modulus and hardness values from the load–displacement curves. A Poisson's ratio of 0.34 was assumed for the coating material in the modulus calculations. These measurements were performed on both the top surface and cross-section of the samples, with a matrix of 25 indents spaced 15 µm apart in both the X and Y directions. The indent spacing was carefully chosen to minimize any strain-field interference between successive indentations. The indents were made using a maximum load of 100 mN with a dwell time of 30 seconds and a loading rate of 160 mN/s. The same methodology was repeated on the unexposed side as well. Additionally, the variation in nanomechanical properties along the cross-section was assessed using a similar approach to microhardness testing, with indentations made across the width of the cross-section, from the exposed coating surface to the unexposed side (refer to Fig. 10). The measurements were conducted on both the top surface and cross-section of the samples, with a matrix of 25 indents spaced 15 µm apart in the X and Y directions (Fig. 10a). The same procedure was applied to the unexposed side of the samples. Additionally, nanomechanical property variations along the cross-section were evaluated similarly to microhardness testing, with indents made across the entire cross-section, from the radiation-exposed surface to the unexposed side (Fig. 10b). This was repeated three times to ensure the accuracy and repeatability of data synthesis. This approach was used to assess the potential effects of radiation penetration and to examine hBN's role in irradiation effects across the coating. The load-displacement response, along with the average nano-hardness and elastic modulus, was documented for all experiments. This method provided a comprehensive understanding of mechanical property gradients across the thickness of the

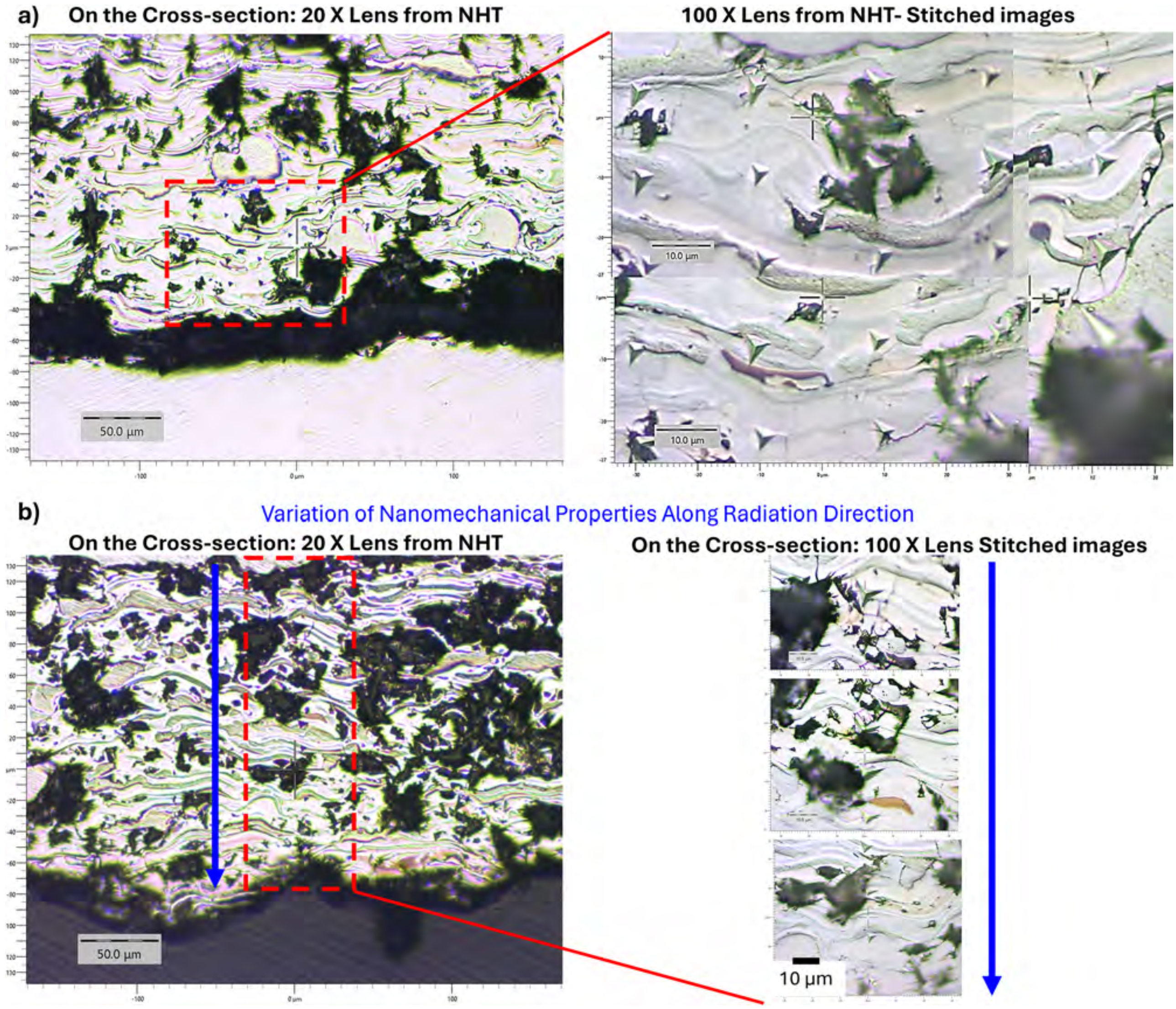

Fig. 10 | Nanoindentation method on coatings to understand nanomechanical properties. a Optical images of indentation matrix on the coating cross-section to assess overall nano-hardness and elastic modulus response of coatings. **b** Indentation line across coating thickness to evaluate nanomechanical response along the direction of radiation travel.

coatings along the direction of radiation travel and atmospheric oxygen diffusion.

To evaluate the statistical significance of the microhardness and nanomechanical measurements, ANOVA was conducted using Origin software with a 95% confidence level. Levene's test for equal variances was applied to confirm homogeneity across the coating regions. Following ANOVA, Tukey's post-hoc means comparison test was performed to identify which specific groups exhibited significant differences in microhardness. Additionally, a power analysis was conducted to assess the sensitivity of the test, ensuring that the sample size was sufficient to detect meaningful differences across the coating layers.

Chemical state and atomic composition of coatings using X-ray photoelectron spectroscopy (XPS)

The atomic composition and chemical state of the coatings were analyzed using XPS and Raman spectroscopy after exposure. A Reinshaw confocal Raman microscope with a 785 nm laser was employed for Raman spectroscopy. A 758 nm laser was used at 5% of 300 mW maximum power. The data collection parameters included a power of 5% of 300 mW, an acquisition time of 10 s, and a total of 1 scan. For XPS analysis, an ESCALAB-250Xi spectrometer operated at room temperature in an ultrahigh vacuum chamber (pressure below 7×10^{-9} mbar) using a monochromatic Al-Kα radiation source, with a power setting of 300 W (15 kV, 20 mA). The beam spot size was set to 650 µm. An electron flood gun was utilized for charge compensation. The sample was mounted on the sample holder using carbon tape. The electron emission angle and the collection angle during XPS analysis were both 90°, as the flat sample surface was oriented perpendicular to the analyzer lens. This configuration allowed optimal signal acquisition for surface-sensitive measurements. The C 1 s peak at 284.8 eV was used as a reference for calibration.

The surface elemental atomic concentration of the samples was determined by deconvoluting the XPS data using OriginLab software. This process involved fitting the individual peaks for each element present in the spectrum. The relative elemental concentrations were calculated by integrating the area under the fitted peaks corresponding to each element, considering the appropriate sensitivity factors. To estimate the elemental composition of the surface, the atomic concentration C_x of a given element x was calculated using the formula[44,45]

$$Atomoic\ Concentration\ of\ Element\ x, C_x = \frac{\frac{I_x}{S_x}}{\sum\left(\frac{I_i}{S_i}\right)} \tag{11}$$

where I_x= Peak area or intensity of element x, S_x = Sensitivity factor of element x, I_i = Peak area intensity of all possible elements I, S_i = Sensitivity factor of all possible elements i. The computation of elemental composition before and after exposure will reveal significant changes in the surface chemistry and elemental distribution, particularly due to the diffusion of atomic oxygen into the sample. These alterations, along with phase transformations in titanium and boron nitride, are critical for understanding the material's behavior under extreme space environmental conditions.

Data availability

The data will be made available on suitable request.

Received: 27 January 2025; Accepted: 14 July 2025;
Published online: 26 July 2025

References

1. Syeda, A. B., Akhlaq, A., Abdul, W., Abdul, M. & Syed, W. H. Development of lightweight aluminum-titanium alloys for aerospace applications. *Key Eng. Mater.* **778**, 22–27 (2018).
2. Zhou, B., Liu, B. & Zhang, S. The advancement of 7xxx series aluminum alloys for aircraft structures: A review. *Metals* **11**, 718–747 (2021).
3. Destefani, J. D. Introduction to titanium and titanium alloys. In *Properties and Selection: Nonferrous Alloys and Special-Purpose Materials* 586–591 https://doi.org/10.31399/asm.hb.v02.a0001080 (ASM International, 1990).
4. Peters, M., Kumpfert, J., Ward, C. H. & Leyens, C. Titanium alloys for aerospace applications. *Adv. Eng. Mater.* **5**, 419–427 (2003).
5. Kunneparambil Sukumaran, A., Zhang, C., Nisar, A. & Agarwal, A. Recent trends in tribological performance of aerospace materials in lunar regolith environment – A critical review. *Adv. Space Res.* **73**, 846–869 (2024).
6. Sukumaran, A. K., Zhang, C., Nisar, A., Rengifo, S. & Agarwal, A. Tribological behavior of Al 6061 and Ti6Al4V alloys against lunar regolith simulants at extreme temperatures. *Wear* **530**, 531 (2023).
7. Williams, J. P., Paige, D. A., Greenhagen, B. T. & Sefton-Nash, E. The global surface temperatures of the moon as measured by the diviner lunar radiometer experiment. *Icarus* **283**, 300–325 (2017).
8. Schwadron, N. A. et al. Lunar radiation environment and space weathering from the Cosmic Ray Telescope for the Effects of Radiation (CRaTER). *J. Geophys. Res. Planets* **117**, 1–13 (2012).
9. Marshall, G. C., Schrader, C. M., Rickman, D. L., Mclemore, C. A. & Fikes, J. C. *Lunar Regolith Simulant User's Guide*. http://www.sti.nasa.gov (2010).
10. Colwell, J. E., Batiste, S., Horányi, M., Robertson, S. & Sture, S. Lunar surface: Dust dynamics and regolith mechanics. *Rev. Geophys.* **45**, 2006 (2007).
11. Ishibashi, K. et al. Wear of Materials by Lunar Regolith Simulant. *J. Jpn. Soc. Tribol.* **55**, 398–405 (2010).
12. *NASA's Management Of The Artemis Missions*. https://oig.nasa.gov/hotline.html (2021).
13. De Oliveira, P. R. et al. Novel polyimide-hexagonal boron nitride nanocomposites for synergistic improvement in tribological and radiation shielding properties. *Tribol. Int.* **189**, 108936 (2023).
14. Kimura, Y., Wakabayashi, T., Okada, K., Wada, T. & Nishikawa, H. Boron nitride as a lubricant additive. *Wear* **232**, 199–206 (1999).
15. Martin, J. M., Le Mogne, T. H., Chassagnette, C. & Gardos, M. N. Friction of hexagonal boron nitride in various environments. *Tribology Trans.* **35**, 462–472 (1992).
16. Chkhartishvili, L., Tabatadze's. G., Nackebia. D., Bzhalava. T., & Kalandadze, I. Hexagonal Boron nitride as a solid lubricant additive (An overview). *Nano Stud.* **14**, 91–98, (2016).
17. Saji, V. S. 2D hexagonal boron nitride (h-BN) nanosheets in protective coatings: A literature review. *Heliyon* **9**, https://doi.org/10.1016/j.heliyon.2023.e19362 (2023).
18. Bacca, N. et al. Tribological and neutron radiation properties of boron nitride nanotubes reinforced titanium composites under lunar environment. *J. Mater. Res.* https://doi.org/10.1557/s43578-022-00708-w (2022).
19. Thibeault, S. A. et al. Nanomaterials for radiation shielding. *MRS Bull*. **40** 836–841 (2015).
20. NIST CENTER FOR NEUTRON RESEARCH: Neutron scattering lengths and cross sections: https://www.ncnr.nist.gov/resources/n-lengths/.
21. Thibeault, S. A. et al. Radiation Shielding Materials Containing Hydrogen, Boron, and Nitrogen: Systematic Computational and Experimental Study-Phase I NIAC FINAL REPORT. 1–29, Report number: HQ-E-DAA-TN33851, (2012).
22. Shang, Y. et al. Multilayer polyethylene/ hexagonal boron nitride composites showing high neutron shielding efficiency and thermal conductivity. *Compos. Commun.* **19**, 147–153 (2020).
23. Kim, S., Ahn, Y., Song, S. H. & Lee, D. Tungsten nanoparticle anchoring on boron nitride nanosheet-based polymer nanocomposites for complex radiation shielding. *Compos Sci. Technol.* **221**, 109353 (2022).
24. Sukumaran, A. K. et al. Tribological and radiation shielding response of novel titanium-boron nitride coatings for lunar structural components. *Surf. Coat. Technol.* **476**, 1–15 (2024).
25. Sukumaran, A. K. et al. Wear and neutron shielding resilience of titanium-hexagonal boron nitride coatings against extreme lunar radiation and thermal cycles. *Surf. Coat. Technol*. **492**, 1–16, (2024).
26. Sukumaran, A. K. et al. Erosion behavior of Ti-hBN multifunctional coatings in a custom-made planetary test rig at extreme lunar temperatures. *Tribol. Int*. 110339, https://doi.org/10.1016/j.triboint.2024.110339 (2024).
27. Allen, C. S., Giraudo, M., Moratto, C. & Yamaguchi, N. Spaceflight environment. In *Space Safety and Human Performance* 87–138 https://doi.org/10.1016/B978-0-08-101869-9.00004-2 (Elsevier, 2017).
28. Low Earth Orbit (LEO) Space Environment Soreq Nuclear Research Center. https://www.gov.il/en/pages/low_earth_orbit (2025).
29. Wu, J. et al. High-entropy (Sm0.2Eu0.2Gd0.2Dy0.2Er0.2)2Hf2O7 ceramic with superb resistance to radiation-induced amorphization. *J. Mater. Sci. Technol.* **155**, 1–9 (2023).
30. Thirsk, R., Kuipers, A., Mukai, C. & Williams, D. The space-flight environment: The international space station and beyond. *CMAJ. Can. Med. Assoc. J*. **180** 1216–1220 (2009).
31. Clark, D. W., Zinkle, S. J., Patel, M. K. & Parish, C. M. High temperature ion irradiation effects in MAX phase ceramics. *Acta Mater.* **105**, 130–146 (2016).
32. Gerasimov, V. V. Effect of irradiation on the mechanical properties of metals. *Atomnaya Energiya*. **66**, 243–244 (1989).
33. Sadeghilaridjani, M. et al. Ion irradiation response and mechanical behavior of reduced activity high entropy alloy. *J. Nucl. Mater.* **529**, 1–7 (2020).
34. Chen, W. Y. et al. Irradiation effects in high entropy alloys and 316H stainless steel at 300 °C. *J. Nucl. Mater.* **510**, 421–430 (2018).
35. Zhu, Y. et al. Microstructural damage evolution of (WTiVNbTa)C5 high-entropy carbide ceramics induced by self-ions irradiation. *J. Eur. Ceram. Soc.* **42**, 2567–2576 (2022).
36. Kumar, N. A. P. K., Li, C., Leonard, K. J., Bei, H. & Zinkle, S. J. Microstructural stability and mechanical behavior of FeNiMnCr high entropy alloy under ion irradiation. *Acta Mater.* **113**, 230–244 (2016).
37. Leyland, A. & Matthews, A. On the significance of the H/E ratio in wear control: a nanocomposite coating approach to optimised tribological behaviour. *Wear* **246**, 1–11(2000).
38. Gaier, J. R. et al. *Degradation of Spacesuit Fabrics in Low Earth Orbit*. NASA/TM—2012-217682, 1–20, http://www.sti.nasa.gov (2012).
39. Wei, W., Meng, C., Fu, Q. & Bao, X. Intercalation-etching of graphene on Pt(111) in H_2 and O_2 observed by in-situ low energy electron microscopy. *Sci. China Chem.* **60**, 656–662 (2017).

40. Yang, Y., Fu, Q., Wei, M., Bluhm, H. & Bao, X. Stability of BN/metal interfaces in gaseous atmosphere. *Nano Res.* **8**, 227–237 (2015).
41. Meng, C. et al. Structural transformation of h-BN overlayers on Pt(111) in oxidative atmospheres. *Phys. Chem. Chem. Phys.* **20**, 11013–11020 (2018).
42. Mungole, M. N., Singh, N. & Mathur, G. N. Oxidation behaviour of Ti6Al4V titanium alloy in oxygen. *Mater. Sci. Technol.* **18**, 111–114 (2002).
43. Greczynski, G. & Hultman, L. A step-by-step guide to perform X-ray photoelectron spectroscopy. *J. Appl. Phys*. **132**, 011101 (2022).
44. Van der Heide, P. *X-Ray Photoelectron Spectroscopy: An Introduction to Principles and Practices*. (Wiley-Blackwell, 2012).
45. Stevie, F. A. & Donley, C. L. Introduction to X-ray photoelectron spectroscopy. *J. Vacuum Sci. Technol. A: Vacuum Surf. Films* **38**, 063204 (2020).
46. Peña-Juárez, M. G. et al. Role of the chemical modification of titanium dioxide surface on the interaction with silver nanoparticles and the capability to enhance antimicrobial properties of poly(lactic acid) composites. *Polym. Bull.* **78**, 2765–2790 (2021).
47. Biesinger, M. C., Lau, L. W. M., Gerson, A. R. & Smart, R. S. C. Resolving surface chemical states in XPS analysis of first row transition metals, oxides and hydroxides: Sc, Ti, V, Cu and Zn. *Appl. Surf. Sci.* **257**, 887–898 (2010).
48. Greczynski, G. & Hultman, L. X-ray photoelectron spectroscopy: Towards reliable binding energy referencing. *Prog. Mater. Sci.* **107**, 100591 (2020).
49. Song, Y. et al. Van der Waals epitaxy and characterization of hexagonal boron nitride nanosheets on graphene. *Nanoscale Res. Lett.* **9**, 1–7 (2014).
50. NIST X-ray Photoelectron Spectroscopy Database (SRD 20), V. 5. 0. https://srdata.nist.gov/xps/.
51. XPS Library. IP-e SF periodic table (Version 3.1)[PDF]. https://xpslibrary.com/wp-content/uploads/2019/09/IP-e-SF-Periodic-Table-Aug-30-2019-v3-1.pdf (2019).
52. NASA Glenn Research Center. MISSE [Web page]. National Aeronautics and Space Administration. https://www1.grc.nasa.gov/space/iss-research/misse/ (2023).

Acknowledgements
The authors sincerely acknowledge the support of the National Aeronautics and Space Administration (NASA) through the 80MSFC21P0018 grant. They also appreciate the use of facilities at the Advanced Materials Engineering Research Institute (AMERI) for conducting this research.

Author contributions
A.K.S. conceptualized the study, curated and analyzed the data, performed formal analysis, conducted the investigation, developed the methodology, and drafted the original manuscript. S.R. administered the project, acquired funding, provided resources, and contributed to the methodology and investigation. W.S. conducted the investigation and contributed to the writing by reviewing and editing the manuscript. A.G. managed project administration and contributed to the investigation. M.F. provided resources, contributed to the methodology, and participated in the investigation. R.T.M. conducted the investigation and curated the data. J.M. participated in the investigation. M.M. supported the project by providing resources and contributing to the investigation. M.R. conducted the investigation, curated the data, and validated the results. S.H.C. contributed to the investigation, validated the results, curated the data, and reviewed and edited the manuscript. C.P. contributed to the methodology, conducted the investigation, validated the results, supervised the work, curated the data, and reviewed and edited the manuscript. A.W. participated in the investigation and validated the results. Y.F. contributed to the investigation and data curation. S.S. contributed to the investigation, curated the data, provided resources, and supervised the work. A.A. conceptualized the study, acquired funding, developed the methodology, conducted the investigation, supervised the work, validated the results, curated the data, and reviewed and edited the manuscript.

Competing interests
The authors declare no competing interests.

Additional information
Supplementary information The online version contains supplementary material available at https://doi.org/10.1038/s41529-025-00644-0.

Correspondence and requests for materials should be addressed to Arvind Agarwal.

Supplementary File

Radiation-Resistant Ti/BN Coatings: Insights from 171 Days Exposure to Space Radiation and Atomic Oxygen in Low Orbit

Abhijith Kunneparambil Sukumaran[1], Sara Rengifo[2], William Scott[2], Annette Gray[2], Miria Finckenor[2], Rony Thomas Murickan[1], Justin McElderry[2], Matthew Mazurkivich[2], Michael Renfro[3], Sang-Hyon Chu[4], Cheol Park[4], Anna Wu[4], Yifei Fu[5], Sudipta Seal[5] and Arvind Agarwal[1,*]

[1]Plasma Forming Laboratory, Florida International University, Miami, FL

[2] Materials Test, Chemistry and Contamination Control Branch, National Aeronautics and Space Administration Marshall Space Flight Centre, Huntsville, AL,

[3] Plasma Processes, LLC, Huntsville, AL

[4]Advanced Materials and Processing Branch, NASA Langley Research Center, Hampton, VA

[5]Advanced Materials Processing and Analysis Centre, Nanoscience Technology Center, University of Central Florida, Orlando, FL

[*] Corresponding Author: Arvind Agarwal, agarwala@fiu.edu, 10555 West Flagler Street, EC 3474, Miami, FL 33174

MISSE-17 Information: Solar cycle data

Temperature change data from underdeck sensor from April to September 2023.

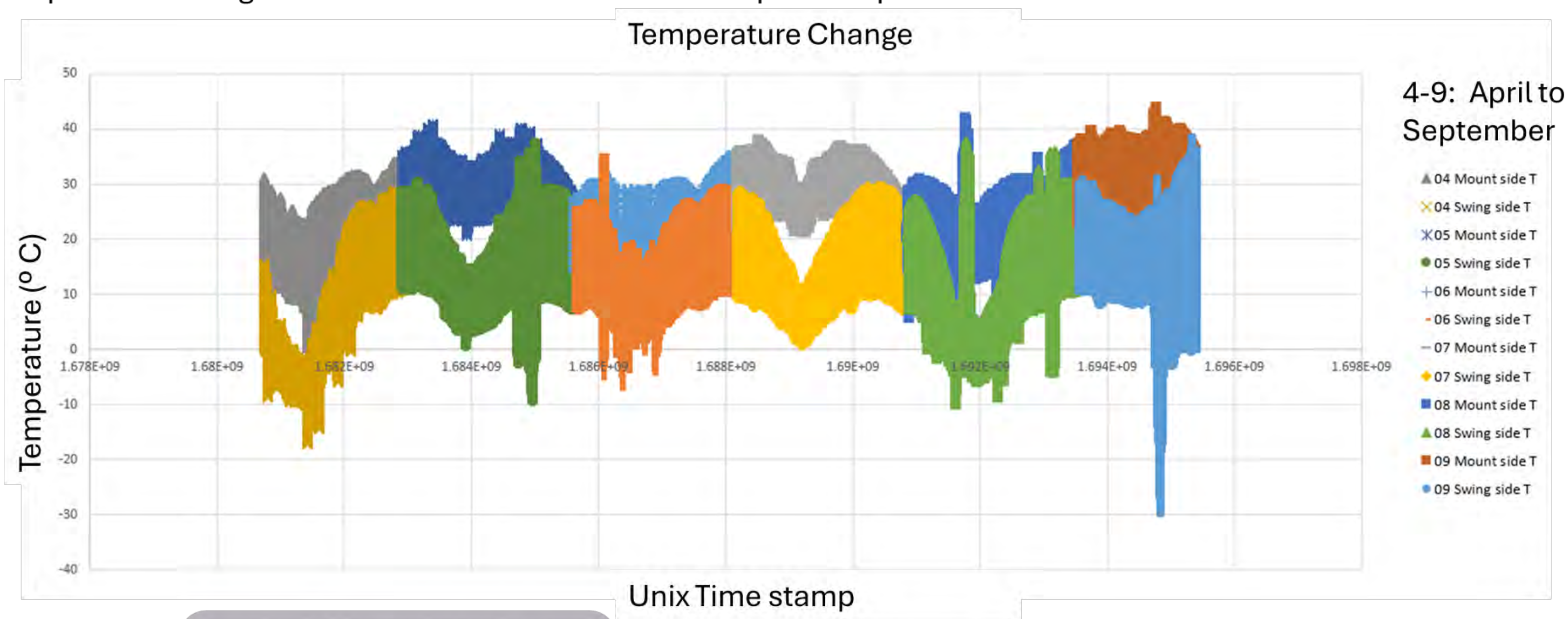

- Highest T: Sep Mount side 43.75°C.
- Lowest T: Sep Swing side -29.75 °C.
- Mount side range (avg): 7-37 °C.
- Swing side range (avg): 0-30 °C.
- From Apr-Sep: avg T increase ~10 °C.

- Less temperature change on mount side.
- Mount side always 5-20 degrees hotter than swing side.
- Follow similar trend every month.
- Steady rise in temperature across the months.

Fig. S1: Temperature cycle data from April to September 2023 from underdeck sensor of MSC flight carrier

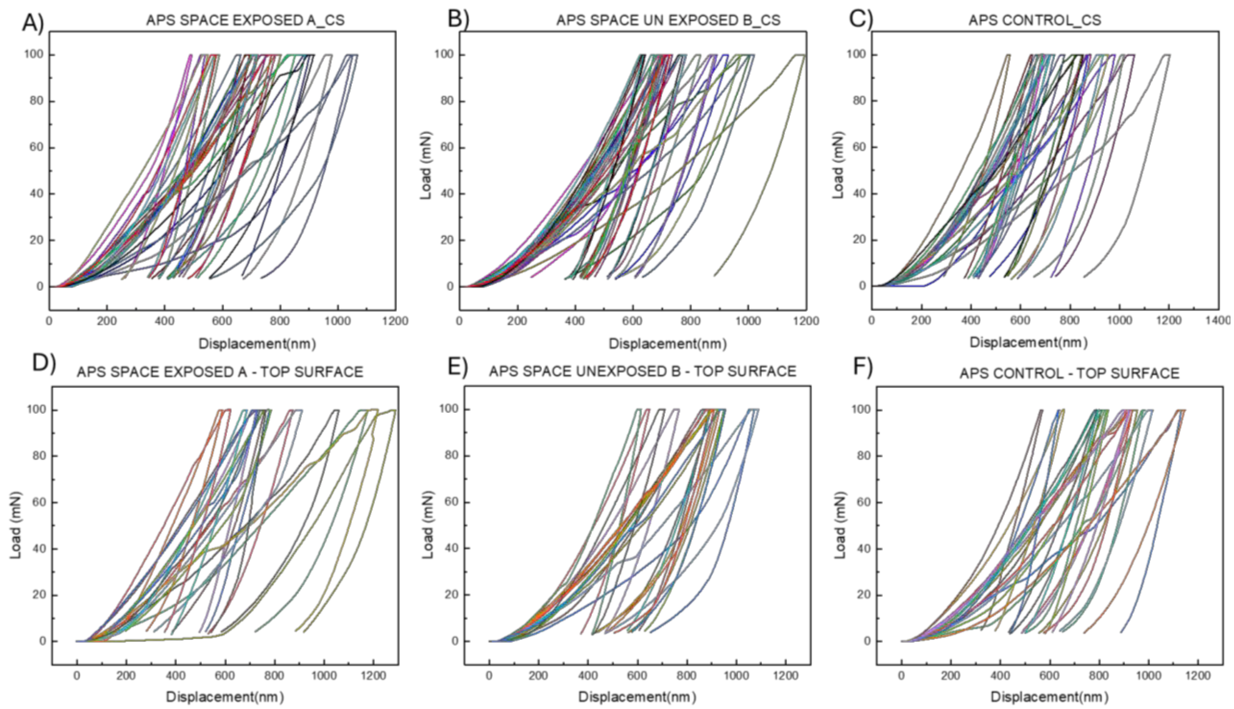

Fig. S2: Load-displacement curves from nanoindentation of APS samples from cross-section A) exposed B) unexposed C) control; and from top surface D) exposed E) unexposed F) control

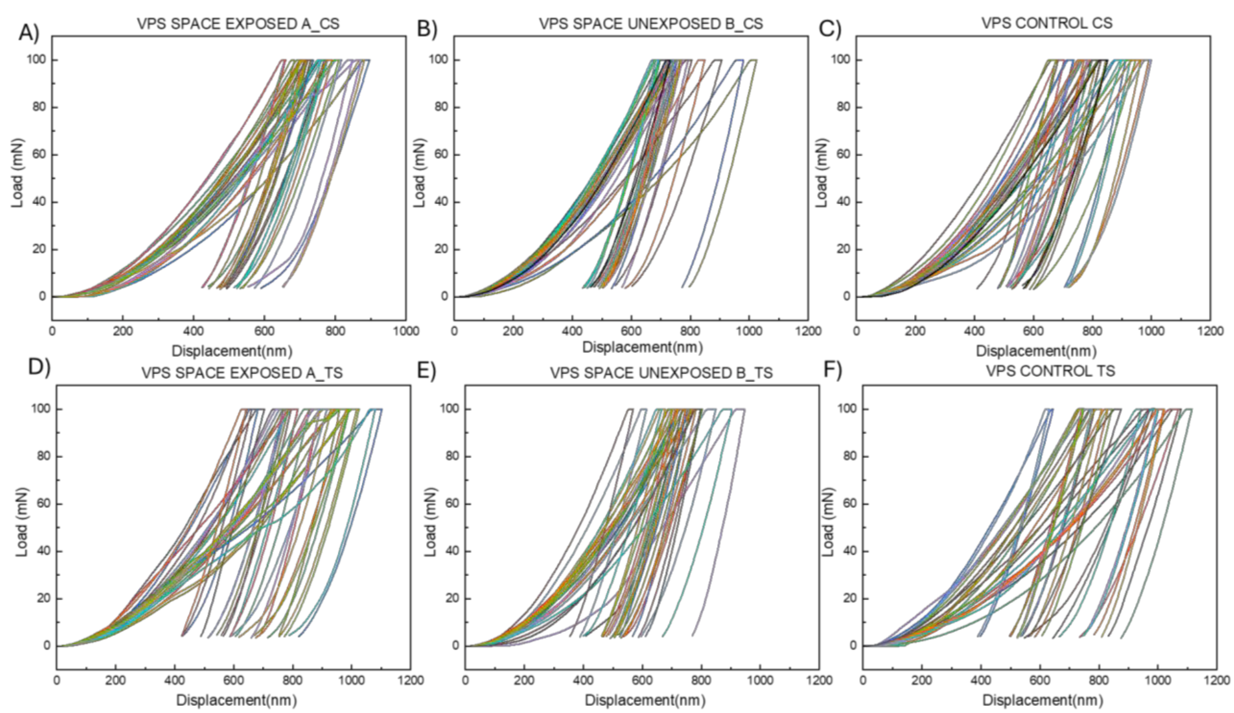

Fig. S3: Load-displacement curves from nanoindentation of VPS samples from top-surface A) exposed B) unexposed C) control; and from top surface D) exposed E) unexposed F) control